



Porosity, mass and geometric imperfection sensitivity in coupled vibration characteristics of CNT-strengthened beams with different boundary conditions

Hossein B. Khaniki¹ · Mergen H. Ghayesh¹ · Shahid Hussain² · Marco Amabili³

Received: 3 September 2020 / Accepted: 27 October 2020 / Published online: 13 November 2020
© Springer-Verlag London Ltd., part of Springer Nature 2020

Abstract

Structures face different types of imperfections and defects during the fabrication process, installation and working environment. In this paper, the imperfection effects in the coupled vibration behaviour of axially functionally graded carbon nanotube (CNT)-strengthened beam structures with different boundary conditions are analysed considering porosity as well as geometric and mass imperfections in the structure. Porosity is modelled using different types of formulations for simple-cell, open-cell and closed-cell porous structures. The porosity is assumed to be either uniform or by varying through the thickness of the hollow beam using different functions. Mass imperfection effect is added to the system by considering a concentrated mass in the system affecting the mass homogeneity of the structure. Geometry imperfection is also considered by having an initial deformation in the structure which could be caused by an improper fabrication process. Coupled axial and transverse equations of motion are obtained using Hamilton's principle and the von Kármán geometrical nonlinearity. Governing equations are solved for different types of boundary conditions using a semi-analytical modal decomposition technique. It is shown that strengthening the base matrix with CNT fibres can improve the vibration behaviour of imperfect structures and the influence of CNT volume fraction and distribution through the length of the beam is discussed. The results provided in this paper may be used as a benchmark to validate future experimental results to prevent imperfection, delamination and stress singularities in the structures.

Keywords Porosity · Geometrical imperfection · Mass imperfection · Porous beam · Imperfect beam · CNT strengthened

1 Introduction

Imperfections in mechanical structures are among the main reasons of inaccuracy in predicting the mechanical behaviour which can lead to high errors and failure of the whole system. Some of the common imperfections which

structures face are porosity, mass imperfection, and geometrical imperfection.

Porosity can be caused by many reasons such as welding and fabrication procedure [1–3] which in some cases is desirable and in some unpleasant. Porosity imperfections are mainly seen when the structures are multi-phase and are manufactured using different elements. Functionally graded (FG) structures are one of the well-known structures, the physical properties of which are varied functionally from a phase to another to obtain advantages of both phases [4–11]; for instance, grading from metal to ceramic to have the strength, deformability of metal and heat resistance of ceramic and different positions of the structure. However, mixing two or more elements in FG structures can cause porosity in the structure which may change the mechanical behaviour of the structure significantly.

In the past few years, porosity in beam structures and their influence on changing the mechanical behaviour of such structures have attracted a lot of attention. For structures

✉ Hossein B. Khaniki
hossein.bakhshikhaniki@adelaide.edu

✉ Mergen H. Ghayesh
mergen.ghayesh@adelaide.edu.au

¹ School of Mechanical Engineering, University of Adelaide, Adelaide, South Australia 5005, Australia

² Faculty of Science and Technology, University of Canberra, Canberra, Australia

³ Department of Mechanical Engineering, McGill University, 817 Sherbrooke Street West, Montreal, Canada

resting on a foundation, Jena et al. [12] studied the vibration behaviour of FG porous beams resting on an elastic foundation. The phase change from ceramic to metal was assumed to be through the thickness direction with uniform porosity. A higher-order beam theory was used to model the structure which was solved via the Navier and Rayleigh–Ritz methods; it was shown that the presence of porosity affects the frequency response differently for ceramic and metal phases. Other studies on beams/plates with different types of porosity can be found in Refs. [13–25], where it was highlighted that the static deformation, buckling and vibration behaviour of structures are significantly impacted by porosities.

For multi-layered FG porous structures, Akbaş et al. [26] examined the dynamic response under pulse loads. Three different types of porosity models (uniform and two symmetric models) were analysed and the FEM results were compared with those of ANSYS; it was shown that porosity in the system leads to softening behaviour and increases the steady-state response of the beam model. Alambeigi et al. [27] investigated the free and forced vibration responses of layered FG beams with the porous core using uniform, symmetric and asymmetric porosities; it was highlighted that higher stiffness was obtained using the symmetric porosity model compare to asymmetric and uniform models. Other studies on the mechanics of layered/sandwich [28–35] FG/porous [36–40] structures (beams, plates and shells) with/without thermal loads [41–46] can be found in literature where it was discussed that increasing the number of layers, properly grading the properties, considering thermal load and porosity, vary the mechanical behaviour of the structure which depending on the characteristics of the structure, these effects vary.

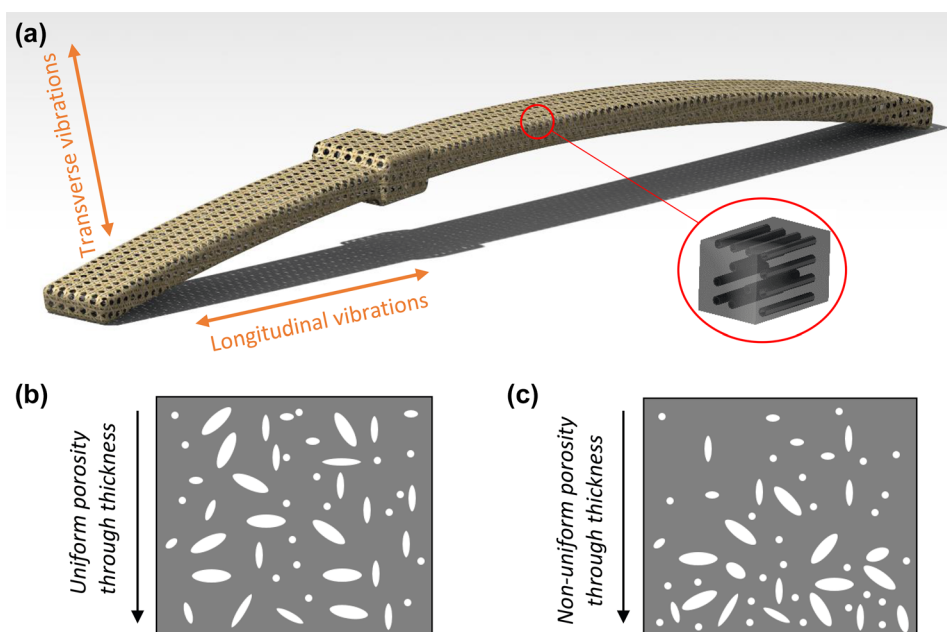
Bi-directional functionally graded (BDFG) beam models with porosity have been examined by Shafiei et al. [47] for small-scale beams. Porosity was assumed to be either uniform or linear-symmetrical variation through the thickness; it was found that the natural frequency terms of the symmetric porous BDFG beam model are larger than those of perfect beam models.

Besides, strengthening base structures with fibres is a method to overcome the weak properties of the base structures along with preventing crack and delamination in the structures. A detailed discussion on CNT-strengthened structures can be found in Ref. [48]; porosity is an unpleasant phenomenon in structures which adding CNT fibres can reduce the pore sizes [49, 50] and cause the porosity by itself as well [51].

Geometrical imperfections can occur in a structure during the fabrication process especially when the structure is made of more than one element (FG structures, layered structures and matrix/fibre structures). In the past few years, researchers have analysed the influence of geometrical imperfections on the vibration response of beam structures [52–58].

However, there is a gap in analysing the porosity as well as geometric and mass imperfection effects on axially functionally graded CNT-strengthened structures in the framework of coupled vibrations. In this study, a comprehensive model for considering different types of imperfection on AFG CNT-strengthened beams is presented for the first time by varying porosity through the thickness and CNT fibre volume fraction through the length for different boundary conditions (Fig. 1 presents a schematic of the current problem). Geometrical imperfection is considered along with mass imperfection and the advantage of having CNT fibres

Fig. 1 Schematic representation of (a) geometrical and mass imperfect porous AFG beam model strengthened with CNT fibres, (b) uniform and (c) non-uniform porosity through the thickness



in overcoming the imperfection in the structure is discussed in detail. Accordingly, this paper is structured as follows: in Sect. 1, an introduction on imperfections and defects in structures is presented by briefly discussing porous beam models in the literature. Section 2 presents a general formulation for imperfect AFG CNT-strengthened beams by presenting five different models of porous variation for simple-, open- and closed-cell structure models. Coupled axial and transverse motion equations are obtained for mass/geometrical imperfect CNT-strengthened structures considering CNT volume fraction variation through the length. Figure 2 shows a schematic of the current problem for different types of boundary conditions. In Sect. 3, coupled equations of motion are transformed to non-dimensional forms and a decomposition technique is presented for solving the equations of motion. In Sect. 4, the current formulation and solution procedure are first verified using an FE simulation software for simplified models and the fast convergence of the method for complicated models is shown for different boundary conditions. After verifying the accuracy of the current methodology, the influence of different types of imperfections on varying both axial and transverse vibration behaviour is discussed in details and the possibility of strengthening the structure and decreasing the defects using CNT fibres and its distribution is discussed. Finally, in Sect. 5, the outcome of this paper is listed and future possible work is discussed. Previously, in Ref. [59], AFG CNT-strengthened beam model was presented and discussed for only transverse vibrations; beam was modelled without any geometrical/mass imperfection and porosity. The equation of

motion was solved for transverse vibration only using generalised differential quadrature method (GDQM) and results for CNT distribution were presented. However, in this study, the vibrations is coupled axially and transversely in the presence of porosity, mass and geometric imperfections, a modal decomposition technique is presented and employed to solve the coupled equations of motion and both coupled axial/transverse vibrations are obtained by considering different types of geometry/mass imperfections, boundary conditions and porosities.

2 Problem formulation

2.1 CNT strengthening and porosity of the beam

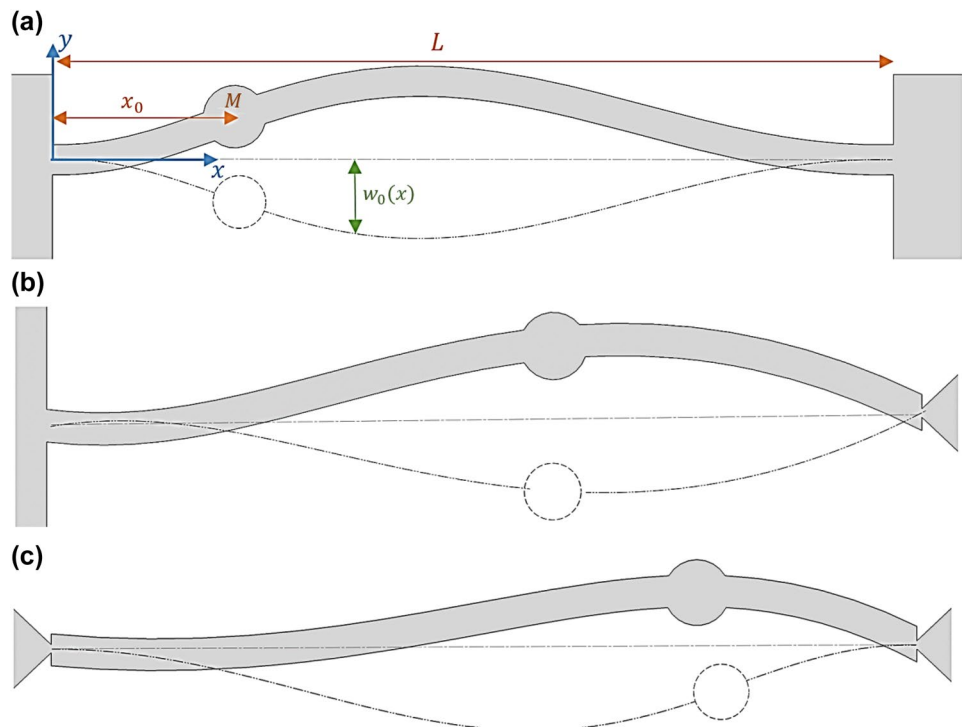
Different models for porosity have been presented by researchers in the past few years. One of the well-known formulations for modelling porosity in multi-phase structures was presented as [60]

$$E(x_i) = -(E_1 - E_2)V_2(x_i) + E_1 - (E_1 + E_2)\frac{\alpha(x_i)}{2}, \quad (1)$$

$$\rho(x_i) = -(\rho_1 - \rho_2)V_2(x_i) + \rho_1 - (\rho_1 + \rho_2)\frac{\alpha(x_i)}{2}, \quad (2)$$

where α is the porosity coefficient term which could vary through any x_i axis following any arbitrary function, subscripts 1 and 2 show different phases of the structure, and

Fig. 2 Geometric and mass imperfect porous axially functionally graded CNT-strengthened beams with (a) clamped–clamped, (b) clamped–pinned, and (c) pinned–pinned boundary conditions



E and ρ are the Young’s modulus and mass density of the structures and V indicates the volume fraction.

Another model used indicates that the magnitude of E and ρ vary differently by having [61]

$$E(x_i) = E_1 [1 - \alpha_1(x_i)], \tag{3}$$

$$\rho(x_i) = \rho_1 [1 - \alpha_2(x_i)]. \tag{4}$$

The main problem with the first model formulation [Eqs. (1) and (2)] is that porosity effect is considered independent from the volume fraction of phases; for instance, if the volume fraction of V_1 is zero, still the effect of porosity in phase 1 part of the structure is considered. In the second model [Eqs. (3) and (4)], the porosity is presented for only one base structure which is useful for isotropic one-phase structures.

Therefore, in this paper, a modified model for AFG CNT-strengthened porous structures is presented by assuming the porosity effects as a function of the volume fraction of each part varying through the thickness direction (z) as

$$E(x, z) = (e_1 E_{\text{CNT}} - E_m) V_{\text{CNT}}(x) + E_m - [E_m V_m(x) + e_1 E_{\text{CNT}} V_{\text{CNT}}(x)] \alpha_1(z), \tag{5}$$

$$\rho(x, z) = (\rho_{\text{CNT}} - \rho_m) V_{\text{CNT}}(x) + \rho_m - [\rho_m V_m(x) + \rho_{\text{CNT}} V_{\text{CNT}}(x)] \alpha_2(z), \tag{6}$$

where e_j is the effective coefficient [59], α_i can take the forms of,

$$\text{Uniform : } \begin{pmatrix} \alpha_1(x_i) \\ \alpha_2(x_i) \end{pmatrix} = \begin{pmatrix} \alpha_{10} \\ \alpha_{20} \end{pmatrix}, \tag{7}$$

$$\text{Parabolic: } \begin{pmatrix} \alpha_1(x_i) \\ \alpha_2(x_i) \end{pmatrix} = \begin{pmatrix} \alpha_{10} \\ \alpha_{20} \end{pmatrix} (1 + x_i)^2, \tag{8}$$

$$\text{Parabolic: } \begin{pmatrix} \alpha_1(x_i) \\ \alpha_2(x_i) \end{pmatrix} = \begin{pmatrix} \alpha_{10} \\ \alpha_{20} \end{pmatrix} (1 + x_i)^2, \tag{9}$$

$$\text{Symmetric: } \begin{pmatrix} \alpha_1(x_i) \\ \alpha_2(x_i) \end{pmatrix} = \begin{pmatrix} \alpha_{10} \\ \alpha_{20} \end{pmatrix} \cos\left(\frac{\pi x_i}{a}\right), \tag{10}$$

$$\text{Non - symmetric: } \begin{pmatrix} \alpha_1(x_i) \\ \alpha_2(x_i) \end{pmatrix} = \begin{pmatrix} \alpha_{10} \\ \alpha_{20} \end{pmatrix} \cos\left(\frac{\pi x_i}{a} - \frac{\pi}{4}\right), \tag{11}$$

through any x_i axis in the general form which in this paper, the porosity is assumed to be through the thickness of the beam ($x_i = z$). The relation between α_{10} and α_{20} is presented for simplified models [60], open-cell solids [61–63] and closed-cell solids [64, 65] as:

$$\text{Simplified models: } \alpha_{20} = \alpha_{10}, \tag{12}$$

$$\text{Open-cell solids: } \alpha_{20} = 1 - \sqrt{1 - \alpha_{10}}, \tag{13}$$

$$\text{Closed-cell cellular: } \alpha_{20} = \frac{1.121 \left(1 - \sqrt[2.3]{1 - \alpha_1(x_i)}\right)}{\left(\frac{\alpha_1(x_i)}{\alpha_{10}}\right)}. \tag{14}$$

Moreover, the distribution of CNT fibre is assumed to vary through the length following a power-law function; therefore, the volume fraction of the base element (m) and the CNT fibres is [59, 66]

$$\begin{cases} V_m(x) = 1 - V_{\text{CNT}}(x), \\ V_{\text{CNT}}(x) = \left(1 - \frac{x}{L}\right)^k V_{\text{CNT-L}} + \left[1 - \left(1 - \frac{x}{L}\right)^k\right] V_{\text{CNT-R}}, \end{cases} \quad 0 \leq x \leq L, \tag{15}$$

where k is the power term, and subscripts L and R indicate the left and right sides of the beam, respectively.

2.2 Geometric and mass imperfect CNT-strengthened porous beam model

By considering the geometrical imperfection of the structure, the strain–deformation and stress–strain behaviour can be modelled using the von Kármán geometrical nonlinearity as

$$\epsilon_{xx} = \frac{\partial u(x, t)}{\partial x} - z \frac{\partial^2 w(x, t)}{\partial x^2} + \frac{1}{2} \left(\frac{\partial w(x, t)}{\partial x} \right)^2 + \left(\frac{\partial w(x, t)}{\partial x} \right) \left(\frac{dw_0(x)}{dx} \right), \tag{16}$$

$$\sigma_{xx} = Q_{11}(x)\epsilon_{xx} = \frac{E_{11}(x)}{1 - \nu^2(x)} \left[\frac{\partial u(x, t)}{\partial x} - z \frac{\partial^2 w(x, t)}{\partial x^2} + \frac{1}{2} \left(\frac{\partial w(x, t)}{\partial x} \right)^2 + \left(\frac{\partial w(x, t)}{\partial x} \right) \left(\frac{dw_0(x)}{dx} \right) \right], \tag{17}$$

where u and w are the axial and transverse displacements and w_0 is the geometrical imperfection of the beam. For the given assumptions, the kinetic (K) and potential (U) energy terms are

$$K = \frac{1}{2} \int_0^L \int_A \rho(x) \left[\left(\frac{\partial w(x, t)}{\partial t} \right)^2 + \left(\frac{\partial u(x, t)}{\partial t} - z \frac{\partial^2 w(x, t)}{\partial x \partial t} \right)^2 \right] + \frac{1}{2} \int_0^L M \left[\left(\frac{\partial w(x, t)}{\partial t} \right)^2 + \left(\frac{\partial u(x, t)}{\partial t} \right)^2 \right] \delta(x - x_0) dA dx, \tag{18}$$

$$U = \frac{1}{2} \int_0^L \int_A \frac{E_{11}(x)}{1 - \nu^2(x)} \left[\frac{\partial u(x, t)}{\partial x} - z \frac{\partial^2 w(x, t)}{\partial x^2} + \frac{1}{2} \left(\frac{\partial w(x, t)}{\partial x} \right)^2 + \left(\frac{\partial w(x, t)}{\partial x} \right) \left(\frac{dw_0(x)}{dx} \right) \right]^2 dA dx, \tag{19}$$

$$\begin{aligned} & -I_0(x) \left(\frac{\partial^2 w(x, t)}{\partial t^2} \right) + I_1(x) \left(\frac{\partial^3 w(x, t)}{\partial x \partial t^2} \right) \\ & + \frac{\partial}{\partial x} \left\{ A_{11}(x) \left[\frac{\partial u(x, t)}{\partial x} + \frac{1}{2} \left(\frac{\partial w(x, t)}{\partial x} \right)^2 + \left(\frac{\partial w(x, t)}{\partial x} \right) \left(\frac{dw_0(x)}{dx} \right) \right] \right\} \\ & - \frac{\partial}{\partial x} \left\{ B_{11}(x) \left[\frac{\partial^2 w(x, t)}{\partial x^2} \right] \right\} - M \left(\frac{\partial^2 u(x, t)}{\partial t^2} \right) \delta(x - x_0) = 0, \end{aligned} \tag{20}$$

$$\begin{aligned} & -I_0(x) \left(\frac{\partial^2 w(x, t)}{\partial t^2} \right) + \frac{\partial}{\partial x} \left[I_2(x) \left(\frac{\partial^3 w(x, t)}{\partial x \partial t^2} \right) \right] - \frac{\partial}{\partial x} \left[I_1(x) \left(\frac{\partial^2 u(x, t)}{\partial t^2} \right) \right] \\ & - \frac{\partial^2}{\partial x^2} \left\{ D_{11}(x) \left[\frac{\partial^2 w(x, t)}{\partial x^2} \right] \right\} - \frac{\partial}{\partial x} \left\{ B_{11}(x) \left[\frac{\partial^2 w(x, t)}{\partial x^2} \right] \left(\frac{\partial w(x, t)}{\partial x} + \frac{dw_0(x)}{dx} \right) \right\} \\ & + \frac{\partial^2}{\partial x^2} \left\{ B_{11}(x) \left[\frac{\partial u(x, t)}{\partial x} + \frac{1}{2} \left(\frac{\partial w(x, t)}{\partial x} \right)^2 + \left(\frac{\partial w(x, t)}{\partial x} \right) \left(\frac{dw_0(x)}{dx} \right) \right] \right\} \\ & + \frac{\partial}{\partial x} \left\{ A_{11}(x) \left[\frac{\partial u(x, t)}{\partial x} + \frac{1}{2} \left(\frac{\partial w(x, t)}{\partial x} \right)^2 \right] \left(\frac{\partial w(x, t)}{\partial x} + \frac{dw_0(x)}{dx} \right) \right\} \\ & + \frac{\partial}{\partial x} \left\{ A_{11}(x) \left[\left(\frac{\partial w(x, t)}{\partial x} \right) \left(\frac{dw_0(x)}{dx} \right) \right] \left(\frac{\partial w(x, t)}{\partial x} + \frac{dw_0(x)}{dx} \right) \right\} \\ & - M \left(\frac{\partial^2 u(x, t)}{\partial t^2} \right) \delta(x - x_0) = 0, \end{aligned} \tag{21}$$

where x_0 is the axial location of the lumped mass M as the representation of mass imperfection, δ is the Dirac delta function and A is the area cross section of the beam (it is assumed that the area cross section is not a function of x). Using Hamilton’s principle [67, 68], one can reach the coupled axial–transverse equations of motion as

where I_0, I_1 and I_2 are the area moments of inertia about the z axis and A_{11}, B_{11} and D_{11} are the stiffness terms defined as,

$$\begin{Bmatrix} I_0(x) \\ I_1(x) \\ I_2(x) \end{Bmatrix} = \int_{-h/2}^{h/2} b [(\rho_{\text{CNT}} - \rho_m) V_{\text{CNT}}(x) + \rho_m - [\rho_m V_m(x) + \rho_{\text{CNT}} V_{\text{CNT}}(x)] \alpha_2(z)] \begin{Bmatrix} 1 \\ z \\ z^2 \end{Bmatrix} dz, \tag{22}$$

$$\begin{Bmatrix} A_{11}(x) \\ B_{11}(x) \\ D_{11}(x) \end{Bmatrix} = \int_{-h/2}^{h/2} b \left[\frac{(e_1 E_{\text{CNT}} - E_m) V_{\text{CNT}}(x) + E_m - [E_m V_m(x) + e_1 E_{\text{CNT}} V_{\text{CNT}}(x)] \alpha_1(z)}{1 - \nu^2(x)} \right] \begin{Bmatrix} 1 \\ z \\ z^2 \end{Bmatrix} dz, \tag{23}$$

where b is the width of the beam which is assumed to be constant.

3 Solution procedure

To solve the coupled motion equations, since the scale of defined terms are considerably different, non-dimensional terms are defined as

$$\begin{aligned} x^* &= \frac{x}{L}, \quad x_0^* = \frac{x_0}{L}, \quad z^* = \frac{z}{h}, \quad w^* = \frac{w}{h}, \quad w_0^* = \frac{w_0}{h}, \quad u^* = \frac{u}{h}, \\ t^* &= t \sqrt{\frac{D_{11,m}}{I_{0,m} L^4}}, \quad \gamma = \sqrt{\frac{L}{h}}, \quad I_0^* = \left(\frac{I_0}{I_{0,m}} \right), \quad I_1^* = \left(\frac{I_1}{I_{0,m} L} \right), \quad I_2^* = \left(\frac{I_2}{I_{0,m} L^2} \right), \\ D_{11}^* &= \frac{D_{11}}{D_{11,m}}, \quad B_{11}^* = \frac{B_{11} h}{D_{11,m}}, \quad A_{11}^* = \frac{A_{11} h^2}{D_{11,m}}, \quad M^* = \frac{M}{I_{0,m} L}. \end{aligned} \tag{24}$$

By assuming small deformations in the system, higher-order deformation terms are neglected and the non-dimensional equations of motion are rewritten as

$$\begin{aligned} & -I_0(x) \left(\frac{\partial^2 u(x,t)}{\partial t^2} \right) + I_1(x) \left(\frac{\partial^3 w(x,t)}{\partial x \partial t^2} \right) \\ & + \frac{\partial}{\partial x} \left\{ A_{11}(x) \left[\gamma^4 \frac{\partial u(x,t)}{\partial x} + \gamma^2 \left(\frac{\partial w(x,t)}{\partial x} \right) \left(\frac{dw_0(x)}{dx} \right) \right] \right\} \\ & - \frac{\partial}{\partial x} \left\{ B_{11}(x) \gamma^2 \left[\frac{\partial^2 w(x,t)}{\partial x^2} \right] \right\} - M \left(\frac{\partial^2 u(x,t)}{\partial t^2} \right) \delta(x - x_0) = 0, \end{aligned} \tag{25}$$

$$\begin{aligned} & -I_0(x) \left(\frac{\partial^2 w(x,t)}{\partial t^2} \right) + \frac{\partial}{\partial x} \left[I_2(x) \left(\frac{\partial^3 w(x,t)}{\partial x \partial t^2} \right) \right] - \frac{\partial}{\partial x} \left[I_1(x) \left(\frac{\partial^2 u(x,t)}{\partial t^2} \right) \right] \\ & - \frac{\partial^2}{\partial x^2} \left\{ D_{11}(x) \left[\frac{\partial^2 w(x,t)}{\partial x^2} \right] \right\} + \frac{\partial^2}{\partial x^2} \left\{ B_{11} \left[\gamma^2 \frac{\partial u(x,t)}{\partial x} + \left(\frac{\partial w(x,t)}{\partial x} \right) \left(\frac{dw_0(x)}{dx} \right) \right] \right\} \\ & - \frac{\partial}{\partial x} \left\{ B_{11}(x) \left[\frac{\partial^2 w(x,t)}{\partial x^2} \frac{dw_0(x)}{dx} \right] \right\} \\ & + \frac{\partial}{\partial x} \left\{ A_{11}(x) \left[\gamma^2 \frac{\partial u(x,t)}{\partial x} \frac{dw_0(x)}{dx} + \left(\frac{\partial w(x,t)}{\partial x} \right) \left(\frac{dw_0(x)}{dx} \right)^2 \right] \right\} \\ & - M \left(\frac{\partial^2 w(x,t)}{\partial t^2} \right) \delta(x - x_0) = 0, \end{aligned} \tag{26}$$

in which $*$ is dropped in Eqs. (25) and (26) for the sake of convenience. It can be seen from Eqs. (25) and (26) that the

linearized non-dimensional equations of motion are coupled due to the geometry imperfection terms and porosity through

the thickness. Using a modal decomposition, the deformations in the system can be presented in a series function as,

$$u = \sum_{j=1}^N \eta_j \varphi_j(x) e^{i\omega t}, \tag{27}$$

$$w = \sum_{j=1}^N \xi_j \tilde{\varphi}_j(x) e^{i\omega t}, \tag{28}$$

and the governing coupled equations of motion can be discretised. Besides, by assuming harmonic response in the system and imperfection as a scale (A_0) of the first mode of vibration, axial and transverse natural frequency terms are obtained via a modal decomposition method [69, 70] where the matrix coefficients K_{ij} and M_{ij} are defined as,

$$K_{11}(l, j) = \gamma^4 \int_0^1 \varphi_l(x) A_{11}(x) \frac{d^2 \varphi_j(x)}{dx^2} + \gamma^4 \int_0^1 \varphi_l(x) \frac{dA_{11}(x)}{dx} \frac{d\varphi_j(x)}{dx} dx, \tag{29}$$

$$\begin{aligned}
 K_{12}(l, j) = & \gamma^2 A_0 \int_0^1 \frac{dA_{11}(x)}{dx} \varphi_l(x) \frac{d\tilde{\varphi}_j(x)}{dx} \frac{d\tilde{\varphi}_1(x)}{dx} dx - \gamma^2 \int_0^1 \varphi_l(x) \frac{dB_{11}(x)}{dx} \frac{d^2 \tilde{\varphi}_j(x)}{dx^2} dx \\
 & + \gamma^2 A_0 \int_0^1 A_{11}(x) \varphi_l(x) \frac{d\tilde{\varphi}_j(x)}{dx} \frac{d^2 \tilde{\varphi}_1(x)}{dx^2} dx + \gamma^2 A_0 \int_0^1 A_{11}(x) \varphi_l(x) \frac{d^2 \tilde{\varphi}_j(x)}{dx^2} \frac{d\tilde{\varphi}_1(x)}{dx} dx \\
 & - \gamma^2 \int_0^1 \varphi_l(x) B_{11}(x) \frac{d^3 \tilde{\varphi}_j(x)}{dx^3} dx,
 \end{aligned} \tag{30}$$

$$\begin{aligned}
 K_{21}(l, j) = & 2\gamma^2 \int_0^1 \frac{dB_{11}(x)}{dx} \tilde{\varphi}_l(x) \frac{d^2 \varphi_j(x)}{dx^2} dx + \gamma^2 A_0 \int_0^1 \frac{dA_{11}(x)}{dx} \tilde{\varphi}_l(x) \frac{d\varphi_j(x)}{dx} \frac{d\tilde{\varphi}_1(x)}{dx} dx \\
 & + \gamma^2 \int_0^1 B_{11}(x) \tilde{\varphi}_l(x) \frac{d^3 \varphi_j(x)}{dx^3} dx + \gamma^2 A_0 \int_0^1 A_{11}(x) \tilde{\varphi}_l(x) \frac{d^2 \varphi_j(x)}{dx^2} \frac{d\tilde{\varphi}_1(x)}{dx} dx \\
 & + \gamma^2 A_0 \int_0^1 A_{11}(x) \tilde{\varphi}_l(x) \frac{d^2 \tilde{\varphi}_1(x)}{dx^2} \frac{d\varphi_j(x)}{dx} dx + \gamma^2 \int_0^1 \frac{d^2 B_{11}(x)}{dx^2} \tilde{\varphi}_l(x) \frac{d\varphi_j(x)}{dx} dx,
 \end{aligned} \tag{31}$$

Table 1 Comparison between modal decomposition and ANSYS natural frequency results (Hz) for transverse vibrations of clamped–clamped isotropic non-porous geometrically perfect beam models with mass imperfection

C–C	Mode	M=0 kg	ANSYS	M=10 kg	ANSYS	M=20 kg	ANSYS
X ₀ =0.3	1	16.54498	16.654	15.25697	15.228	14.16834	14.256
	2	45.53588	45.468	40.36990	39.961	37.59152	37.517
	3	89.05181	88.582	86.15985	86.076	84.94882	84.49
X ₀ =0.4	1	16.54498	16.654	14.49581	14.589	13.02662	13.107
	2	45.53588	45.468	43.13506	43.019	41.84945	41.676
	3	89.05181	88.582	87.32389	86.05	86.38937	84.744
X ₀ =0.5	1	16.54498	16.654	14.20903	14.301	12.63347	12.713
	2	45.53588	45.468	45.53588	45.355	45.53588	45.24
	3	89.05181	88.582	81.06108	80.238	77.22323	76.393

Table 2 Comparison between modal decomposition and ANSYS natural frequency results (Hz) for transverse vibrations of pinned–pinned isotropic non-porous geometrically perfect beam models with mass imperfection

P–P	Mode	M=0 kg	ANSYS	M=10 kg	ANSYS	M=20 kg	ANSYS
X ₀ =0.3	1	7.299368	7.2937	6.702680	6.6974	6.222592	6.2176
	2	29.15756	29.064	26.46747	26.385	24.92880	24.844
	3	65.45570	64.963	64.85182	64.179	64.53172	63.669
X ₀ =0.4	1	7.299368	7.2937	6.516071	6.5116	5.936170	5.9323
	2	29.15756	29.064	28.08131	27.967	27.41953	27.28
	3	65.45570	64.963	63.12118	62.489	61.77384	60.963
X ₀ =0.5	1	7.299368	7.2937	6.449979	6.4459	5.839414	5.8361
	2	29.15756	29.064	29.15756	29.02	29.15756	28.975
	3	65.45570	64.963	59.21094	58.77	55.96950	55.51

Table 3 Comparison between modal decomposition and ANSYS natural frequency results (Hz) for transverse vibrations of clamped–pinned isotropic non-porous geometrically perfect beam models with mass imperfection

C–P	Mode	$M=0$ kg	ANSYS	$M=10$ kg	ANSYS	$M=20$ kg	ANSYS
$X_0=0.3$	1	11.40214	11.442	10.85069	10.89	10.34649	10.386
	2	36.89672	36.833	32.47127	32.412	29.77571	29.700
	3	76.80116	76.137	72.65092	71.854	70.85106	69.879
$X_0=0.5$	1	11.40214	11.442	10.02127	10.058	9.036036	9.0692
	2	36.89672	36.833	36.24040	36.105	35.82365	35.621
	3	76.80116	76.137	70.74049	70.109	67.72722	67.034
$X_0=0.7$	1	11.40214	11.442	10.13585	10.168	9.196766	9.2234
	2	36.89672	36.833	34.29688	34.241	32.90268	32.836
	3	76.80116	76.137	76.75441	75.759	76.72843	75.27

Table 4 Comparison between modal decomposition and ANSYS natural frequency results (Hz) for transverse/axial vibrations of clamped–clamped AFG CNT-strengthened non-porous geometrically perfect beam models with mass imperfection

C–C	Mode	$M=0$ kg	ANSYS	$M=20$ kg	ANSYS	$M=40$ kg	ANSYS
Transverse vibration mode							
$X_0=0.3$	1	65.45766	65.47	54.23521	54.436	46.94808	47.179
	2	180.6386	179.18	152.0502	150.2	142.5023	140.4
Axial vibration mode							
$X_0=0.3$	1	1002.068	958.64	840.0320	764.11	682.6930	640.53
	2	2025.172	1917.3	1768.550	1672.7	1689.980	1577.7
Transverse vibration mode							
$X_0=0.5$	1	65.45766	65.47	50.34475	50.302	42.34610	42.285
	2	180.6386	179.18	178.8222	177.74	178.0160	177.09
Axial vibration mode							
$X_0=0.5$	1	1002.068	958.64	792.0218	759.75	670.2931	639.36
	2	2025.172	1917.3	1974.037	1852.4	1946.530	1788.4
Transverse vibration mode							
$X_0=0.3$	1	65.45766	65.47	57.92392	57.686	52.02157	51.647
	2	180.6386	179.18	148.4752	147.37	135.6000	134.75
Axial vibration mode							
$X_0=0.7$	1	1002.068	958.64	878.1353	832.73	775.0976	726.31
	2	2025.172	1917.3	1681.209	1579.9	1554.255	1449.3

$$\begin{aligned}
 K_{22}(l, j) = & - \int_0^1 \tilde{\varphi}_l(x) \frac{d^2 D_{11}(x)}{dx^2} \frac{d^2 \tilde{\varphi}_j(x)}{dx^2} dx + 2A_0^2 \int_0^1 \tilde{\varphi}_l(x) A_{11}(x) \frac{d\tilde{\varphi}_j(x)}{dx} \frac{d\tilde{\varphi}_l(x)}{dx} \frac{d^2 \tilde{\varphi}_1(x)}{dx^2} dx \\
 & + A_0 \int_0^1 \tilde{\varphi}_l(x) \frac{d^2 B_{11}(x)}{dx^2} \frac{d\tilde{\varphi}_j(x)}{dx} \frac{d\tilde{\varphi}_l(x)}{dx} dx + A_0 \int_0^1 \tilde{\varphi}_l(x) B_{11}(x) \frac{d\tilde{\varphi}_j(x)}{dx} \frac{d^3 \tilde{\varphi}_1(x)}{dx^3} dx \\
 & + A_0 \int_0^1 \tilde{\varphi}_l(x) \frac{dB_{11}(x)}{dx} \frac{d^2 \tilde{\varphi}_j(x)}{dx^2} \frac{d\tilde{\varphi}_l(x)}{dx} dx + 2A_0 \int_0^1 \tilde{\varphi}_l(x) \frac{dB_{11}(x)}{dx} \frac{d\tilde{\varphi}_j(x)}{dx} \frac{d^2 \tilde{\varphi}_1(x)}{dx^2} dx \\
 & - 2 \int_0^1 \tilde{\varphi}_l(x) \frac{dD_{11}(x)}{dx} \frac{d^3 \tilde{\varphi}_j(x)}{dx^3} dx + A_0 \int_0^1 \tilde{\varphi}_l(x) B_{11}(x) \frac{d^2 \tilde{\varphi}_j(x)}{dx^2} \frac{d^2 \tilde{\varphi}_1(x)}{dx^2} dx \\
 & + A_0^2 \int_0^1 \tilde{\varphi}_l(x) \frac{dA_{11}(x)}{dx} \frac{d\tilde{\varphi}_j(x)}{dx} \left(\frac{d\tilde{\varphi}_l(x)}{dx} \right)^2 dx - \int_0^1 \tilde{\varphi}_l(x) D_{11}(x) \frac{d^4 \tilde{\varphi}_j(x)}{dx^4} dx \\
 & + A_0^2 \int_0^1 \tilde{\varphi}_l(x) A_{11}(x) \frac{d^2 \tilde{\varphi}_j(x)}{dx^2} \left(\frac{d\tilde{\varphi}_l(x)}{dx} \right)^2 dx,
 \end{aligned} \tag{32}$$

Table 5 Comparison between modal decomposition and ANSYS natural frequency results (Hz) for transverse/axial vibrations of simply supported AFG CNT-strengthened non-porous geometrically perfect beam models with mass imperfection

P-P	Mode	M=0 kg	ANSYS	M=20 kg	ANSYS	M=40 kg	ANSYS
Transverse vibration mode							
X ₀ =0.3	1	29.27224	29.264	24.62097	24.626	21.59304	21.604
	2	116.3363	116.07	100.6153	100.2	94.48223	94.019
Axial vibration mode							
X ₀ =0.3	1	952.7078	957.26	767.4379	762.54	680.1441	639.58
	2	1910.283	1914.5	1714.302	1671.5	1647.493	1577.5
Transverse vibration mode							
X ₀ =0.5	1	29.27224	29.264	23.49565	23.483	20.16564	20.151
	2	116.3363	116.07	115.8651	115.63	115.6187	115.4
Axial vibration mode							
X ₀ =0.5	1	952.7078	957.26	763.9377	758.95	650.7854	638.8
	2	1910.283	1914.5	1857.427	1848.7	1828.645	1785.1
Transverse vibration mode							
X ₀ =0.7	1	29.27224	29.264	25.34383	25.317	22.59212	22.557
	2	116.3363	116.07	99.21084	98.937	92.09834	91.822
Axial vibration mode							
X ₀ =0.7	1	952.7078	957.26	836.0688	831.9	739.6047	725.79
	2	1910.283	1914.5	1607.139	1577.7	1490.695	1447.0

Table 6 Comparison between modal decomposition and ANSYS natural frequency results (Hz) for transverse/axial vibrations of clamped simply supported AFG CNT-strengthened non-porous geometrically perfect beam models with mass imperfection

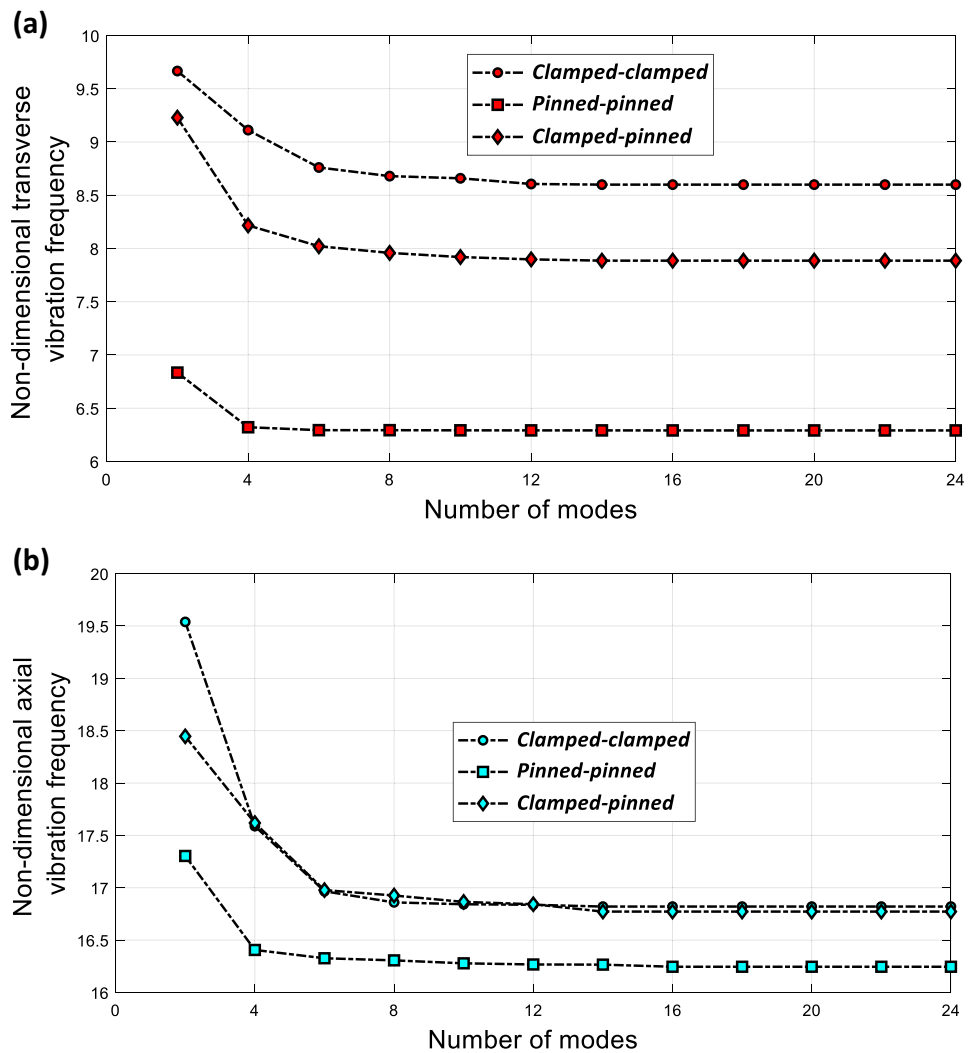
C-P	Mode	M=0 kg	ANSYS	M=20 kg	ANSYS	M=40 kg	ANSYS
Transverse vibration mode							
X ₀ =0.3	1	43.76022	44.106	38.78227	39.174	34.96295	35.354
	2	145.1754	145.24	117.3377	117.07	106.4362	105.93
Axial vibration mode							
X ₀ =0.3	1	989.3234	958.64	796.6410	764.11	676.1579	640.53
	2	1982.381	1917.3	1730.486	1672.7	1654.463	1577.7
Transverse vibration mode							
X ₀ =0.5	1	43.76022	44.106	34.55089	34.815	29.41392	29.631
	2	145.1754	145.24	144.0274	143.91	143.4597	143.25
Axial vibration mode							
X ₀ =0.5	1	989.3234	958.64	786.2982	759.75	667.3437	639.36
	2	1982.381	1917.3	1949.808	1852.4	1930.514	1788.4
Transverse vibration mode							
X ₀ =0.7	1	43.76022	44.106	36.12708	36.336	31.34248	31.486
	2	145.1754	145.24	127.5133	127.68	120.8768	121.08
Axial vibration mode							
X ₀ =0.7	1	989.3234	958.64	859.6768	832.73	755.6723	726.31
	2	1982.381	1917.3	1664.560	1579.9	1548.265	1449.3

$$M_{11}(l, j) = \int_0^1 I_0(x)\varphi_l(x)\varphi_j(x)dx + M \int_0^1 \varphi_l(x)\varphi_j(x)\delta(x - x_0)dx, \tag{33}$$

$$M_{21}(l, j) = \int_0^1 I_1(x)\tilde{\varphi}_l(x)\frac{d\varphi_j(x)}{dx}dx + \int_0^1 \frac{dI_1(x)}{dx}\tilde{\varphi}_l(x)\varphi_j(x)dx, \tag{35}$$

$$M_{12}(l, j) = - \int_0^1 I_1(x)\varphi_l(x)\frac{d\tilde{\varphi}_j(x)}{dx}dx, \tag{34}$$

Fig. 3 Convergence of the coupled axial/transverse vibration results by increasing the number of assumed modes for different boundary conditions: (a) transverse vibration; (b) axial vibration



$$\begin{aligned}
 M_{22}(l, j) = & \int_0^1 I_0(x) \tilde{\varphi}_l(x) \tilde{\varphi}_j(x) dx - \int_0^1 I_2(x) \tilde{\varphi}_l(x) \frac{d^2 \tilde{\varphi}_j(x)}{dx^2} dx \\
 & - \int_0^1 \frac{dI_2(x)}{dx} \tilde{\varphi}_l(x) \frac{d\tilde{\varphi}_j(x)}{dx} dx + M \int_0^1 \tilde{\varphi}_l(x) \tilde{\varphi}_j(x) \delta(x - x_0) dx.
 \end{aligned}
 \tag{36}$$

By solving the discretised non-dimesnional coupled equations of motion, the vibration response of the system can be obtained.

4 Results and discussion

A general formulation for AFG CNT-strengthened beams with different kinds of porosity, geometric and mass imperfections was formulated in the previous section. In this section, the results for the axial and transverse frequencies are obtained and presented via formulations of the previous

section and the sensitivity of the system to different types of mass/geometric imperfections and porosities is discussed. Moreover, for simpler models where there is no geometric and porous imperfections, the accuracy and convergence of the current methodology are verified using FE modelling and the influence of different types of imperfection on the vibration response of the non-porous system is discussed. Simplified model of the problem is simulated as homogeneous or AFG CNT-strengthened non-porous geometrically perfect beams with a mass imperfection using ANSYS [71] and comparison with the current methodology is presented in the next subsection for different types of boundary conditions.

4.1 Verification and comparison

For the sake of verification, homogeneous and AFG CNT-strengthened non-porous geometrically perfect beams with

Fig. 4 Uniform porosity imperfection effect in varying the fundamental transverse vibration frequency term for simple-cell and closed-cell models: (a) clamped–pinned; (b) pinned–pinned; (c) clamped–clamped

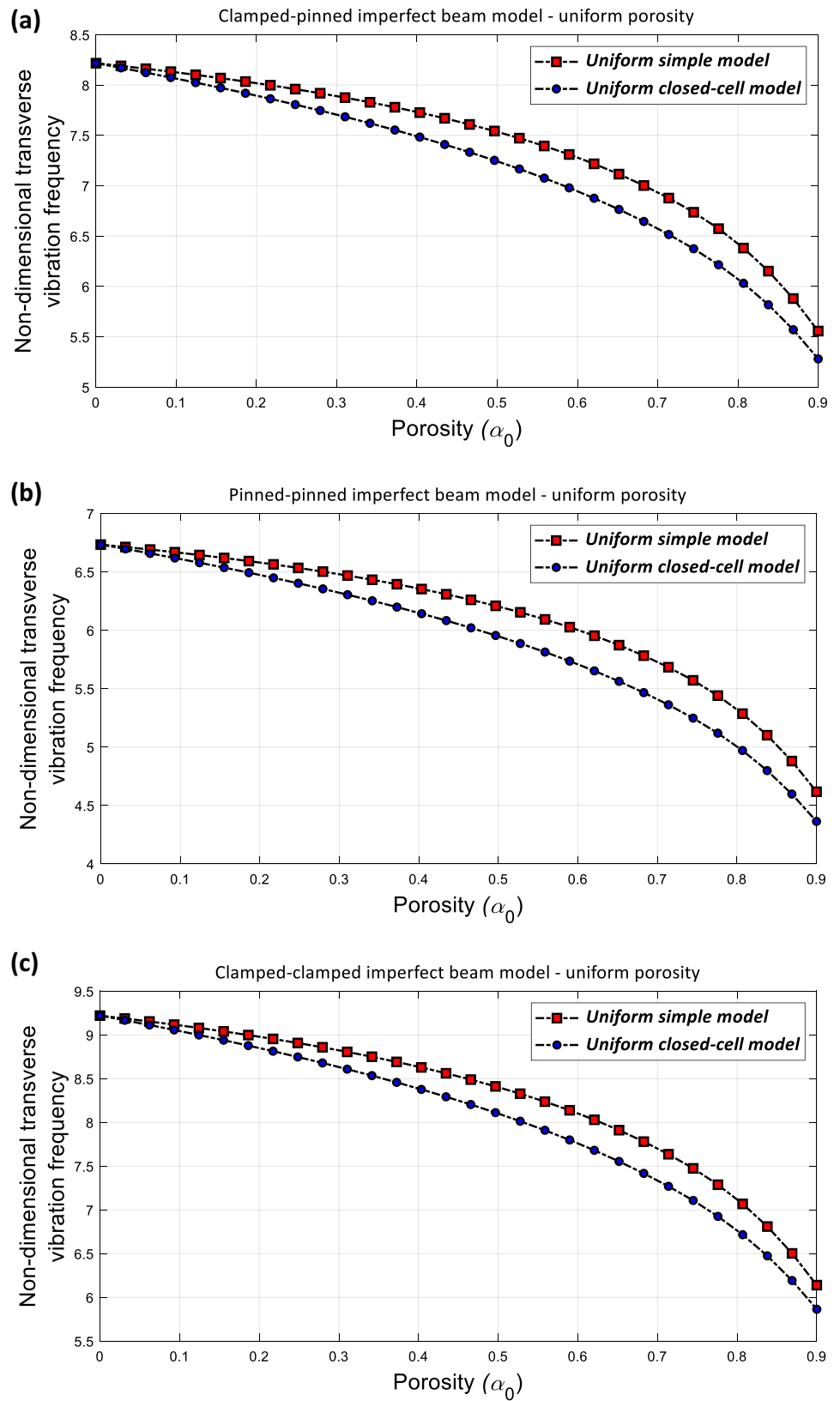


Fig. 5 Uniform porosity imperfection effect in varying the fundamental axial vibration frequency term for simple-cell and closed-cell models: (a) clamped–pinned; (b) pinned–pinned; (c) clamped–clamped

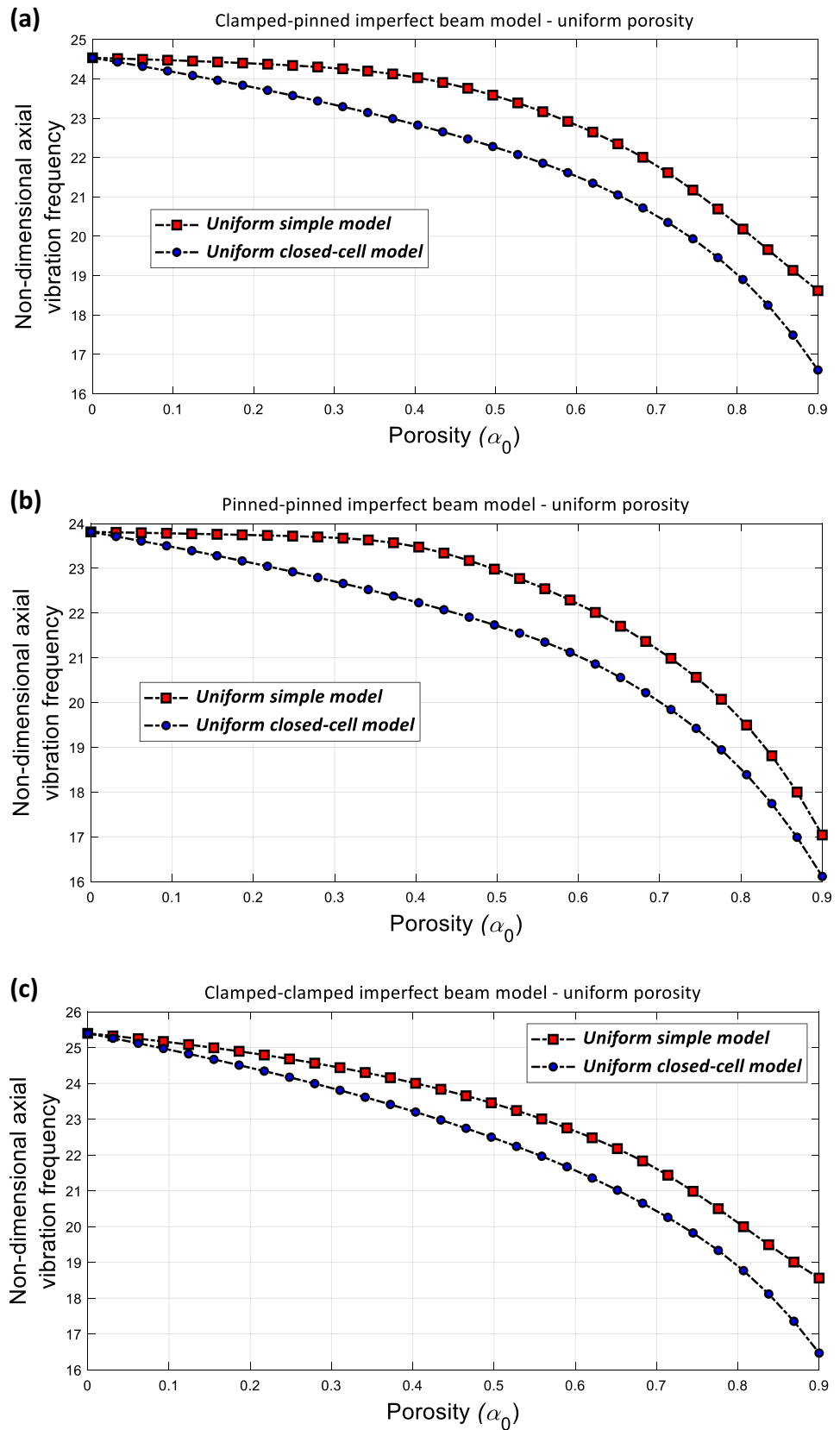
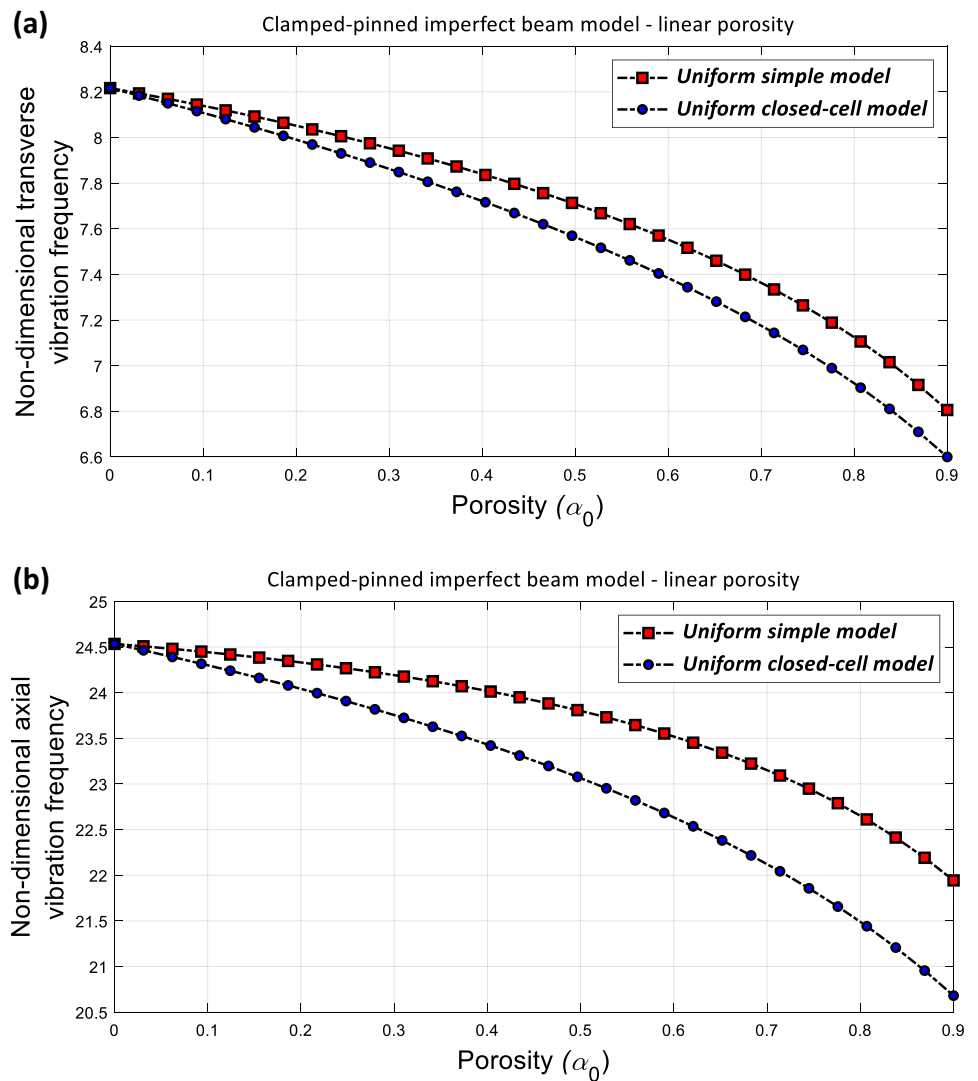


Fig. 6 Linear porosity imperfection effect in varying the fundamental vibration frequencies for simple-cell and closed-cell clamped–pinned models: (a) transverse vibration; (b) axial vibration

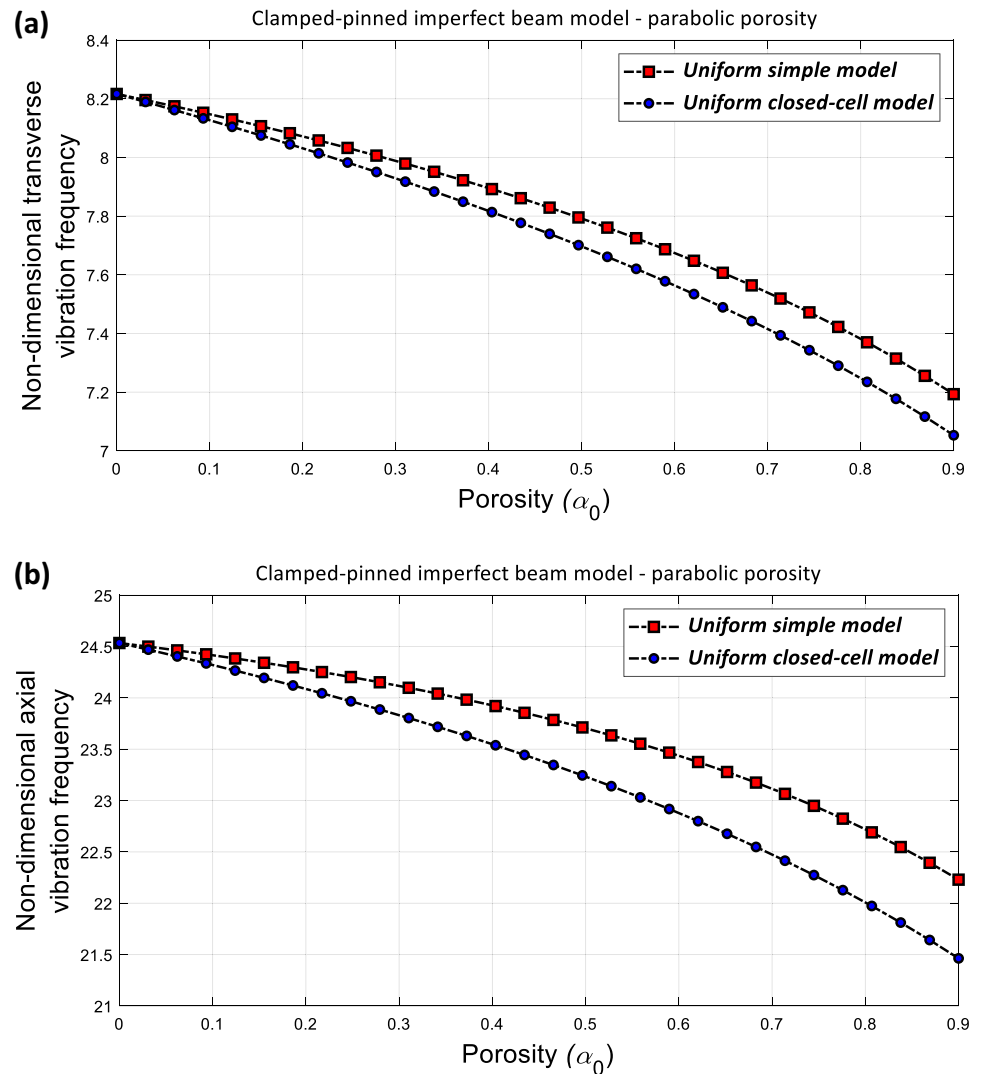


a concentrated mass in a certain distance from the left end of the beam is simulated using ANSYS [71] and the results are compared with those based on the current methodology. By having geometrical properties as $L=3$ m, $h=0.1$ m, $b=0.2$ m, and physical properties as $\rho_m = 1190$ kg/m³, $\rho_{CNT} = 1400$ kg/m³, $E_m = 2.5$ GPa, $E_{CNT} = 5646.6$ GPa, $e_1 = 0.14$, $\nu = 0.3$, results for the first three fundamental natural frequency terms are presented in Tables 1, 2 and 3 for isotropic beams and are compared to those obtained by ANSYS for clamped–clamped, pinned–pinned and clamped–pinned boundary conditions, respectively, for simpler models where there is no geometric and porous imperfections. Besides, by assuming AFG CNT fibre distribution through the base matrix by having $V_{CNT, total} = 5\%$ and $V_{CNT, left} = 2.5\%$, the first three natural frequency terms are calculated and compared with ANSYS. Tables 4, 5 and

6 show the first two frequency terms for axial and transverse dynamics of the mentioned AFG CNT-strengthened non-porous geometrically perfect beam with mass imperfection in different positions for clamped–clamped, pinned–pinned and clamped–pinned boundary conditions, respectively. It can be seen that the results are in a good agreement for all the boundary conditions for both homogeneous and AFG CNT-strengthened beam models.

Moreover, to show the convergence of the current solution method, fundamental frequencies for different boundary conditions and the total number of modes are calculated. The frequency results are shown in Fig. 3a, b for fundamental transverse and axial frequencies, respectively, with $V_{CNT, total} = 5\%$, $V_{CNT, left} = 2.5\%$, $k = 1$, $A_0 = 0.5$, $\alpha_{10} = 0.4$ (uniform open cell model), $M = 10$ kg, $x_0 = 0.3$, $L = 1$ m, $h = 0.1$ m; it can be seen that increasing the total number of

Fig. 7 Parabolic porosity imperfection effect in varying the fundamental vibration frequencies for simple-cell and closed-cell clamped–pinned models: (a) transverse vibration; (b) axial vibration



modes leads to convergence in the results for all the boundary conditions and therefore, for the further calculations, ten modes for the coupled dynamics are considered.

4.2 Influence of porosity imperfection

After verifying the current methodology, the influence of porosity imperfection on the coupled vibration behaviour of AFG CNT-strengthened beams is presented in this section. A beam with the length of 2 m, thickness 10 cm is assumed with a concentrated mass of 15 kg at $x_0 = 0.4$. The beam is strengthened using CNT fibres by having $V_{\text{CNT, total}} = 5\%$ and $V_{\text{CNT, left}} = 1\%$ and $k = 1$ and other properties are as mentioned in the previous section. For this model, porosity is presented uniformly through the thickness ($\alpha_1 = \alpha_{10}$) for simplified models, open-cell models and closed-cell

models. Fundamental natural frequency terms for transverse dynamics are presented in Fig. 4a–c for clamped–pinned, pinned–pinned and clamped–clamped boundary conditions, respectively, and for axial vibrations in Fig. 5a–c. It can be seen that increasing the uniform porosity leads to lower fundamental axial and transverse vibration frequencies and simple-cell model gives higher-frequency terms for all the porosity models and boundary conditions.

Similarly, for linear and parabolic variation of porosity through the beam thickness, the axial and transverse fundamental frequency parameters are shown in Figs. 6 and 7, respectively. It can be seen that changing the porosity from uniform to linear and parabolic models, the same trend of stiffness softening behaviour is observed.

By comparing the fundamental frequency terms for axial and transverse vibrations in Fig. 8a–d, it can be seen that for

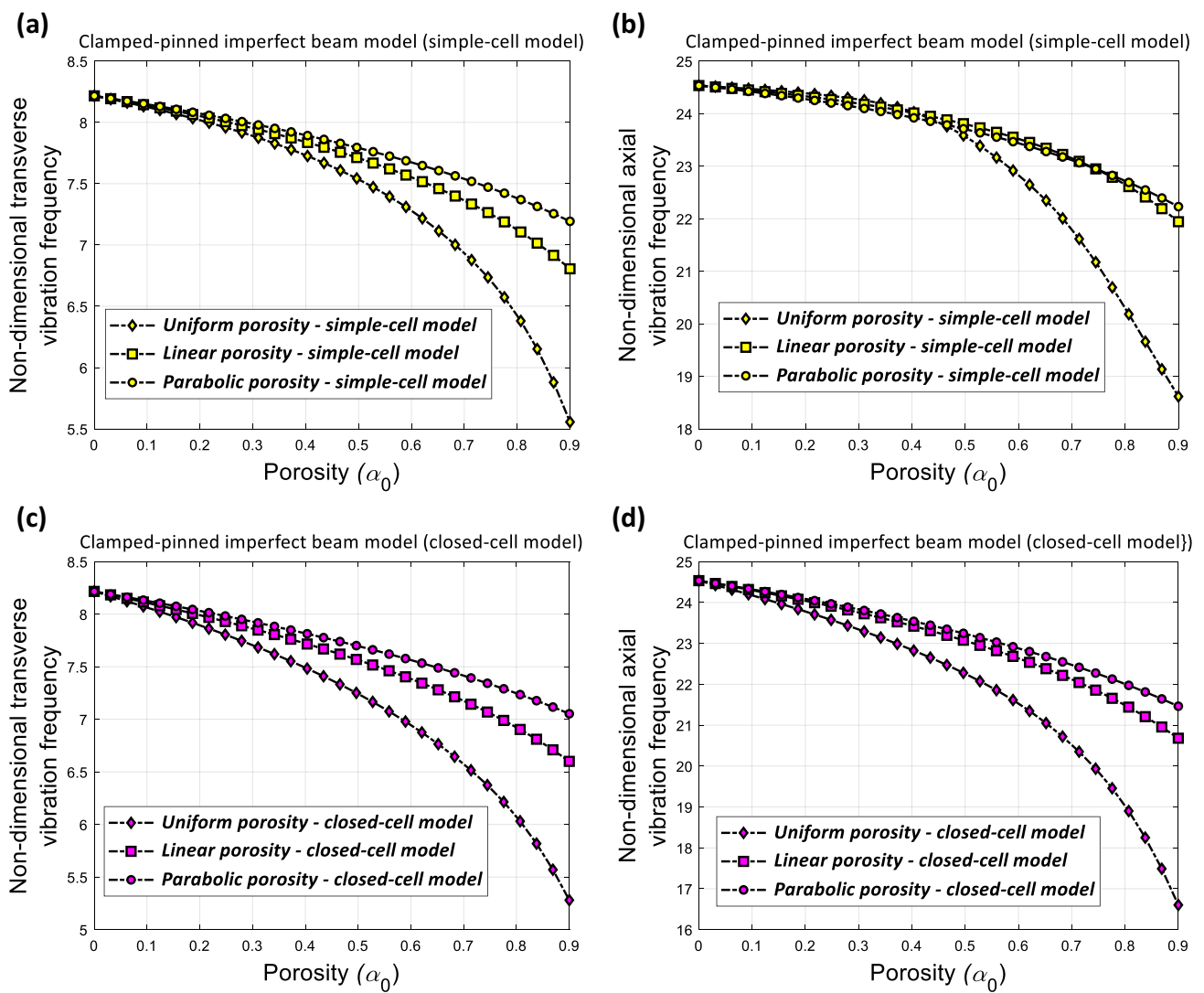


Fig. 8 Influence of varying the porosity model on the vibration response: (a) transverse vibration of the simple-cell model; (b) axial vibration of the simple-cell model; (c) transverse vibration of the closed-cell model; (d) axial vibration of the closed-cell model

the simple-cell model, changing the porosity model from uniform to linear and parabolic, the fundamental frequency terms increase for both the cell models.

4.3 Influence of mass imperfection

In studying the influence of mass imperfection, the position and the mass weight play the dominant role. Accordingly, the previous beam model is considered for closed-cell porosity model and different boundary conditions. Figures 9 and 10 show the variation of the fundamental natural frequency terms for the first three vibration modes of linear

and symmetric pinned–pinned porous models, respectively. Similarly, results for clamped–pinned and clamped–clamped beam models are presented in Figs. 11, 12 and 13. It can be seen that the first mode of vibration is highly sensitive to mass imperfection around the middle of the beam, while the second mode is more sensitive to mass around a quarter length.

To have a better understanding of the influence of porous imperfection on the mass sensing of the structure, Fig. 14 shows the variation of the fundamental frequency terms for different mass and position which shows that symmetric porous model shows more sensitivity to mass imperfection and this sensitivity becomes close to linear porous model by increasing the mass of the imperfection.

Fig. 9 Influence of mass imperfection on the first three vibration modes of the pinned–pinned linear porous model: (a) first natural frequency; (b) second natural frequency; (c) third natural frequency

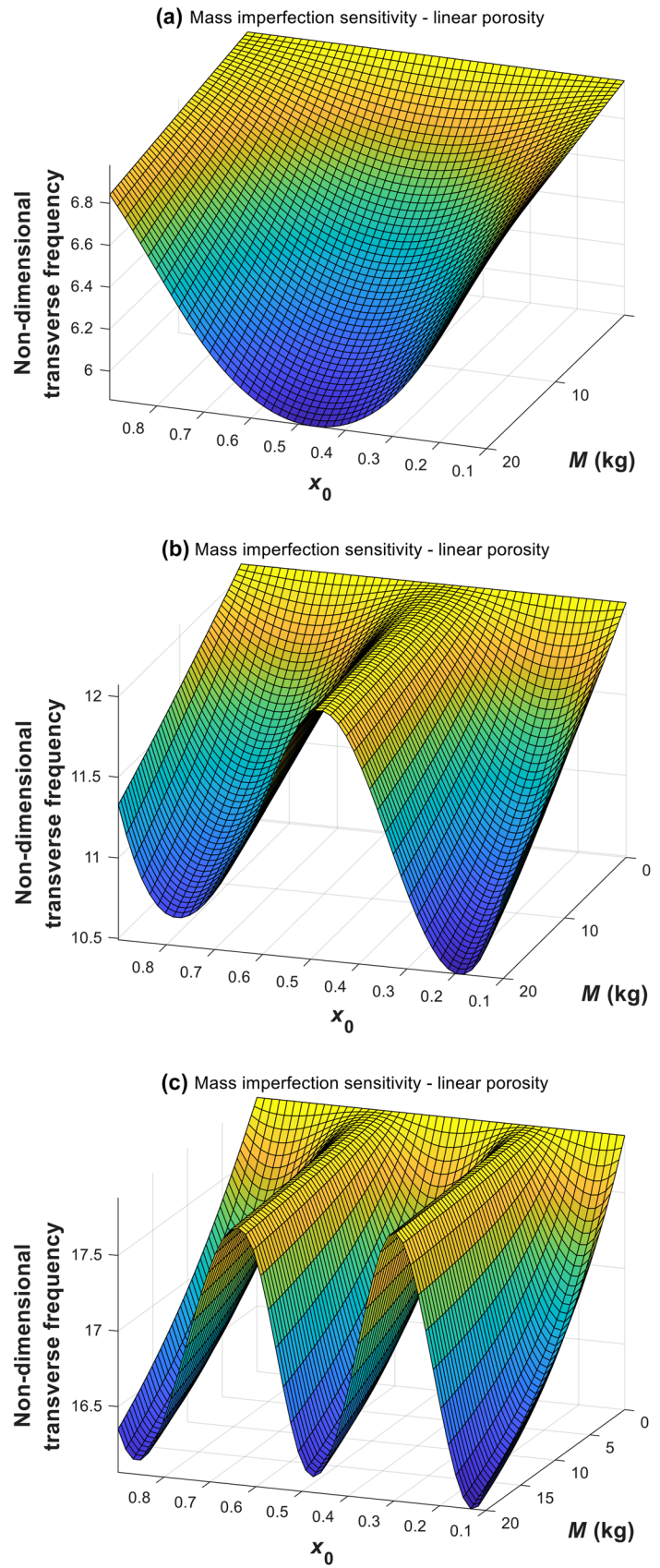


Fig. 10 Influence of mass imperfection on the first three vibration modes of the pinned–pinned symmetric porous model: (a) first natural frequency; (b) second natural frequency; (c) third natural frequency

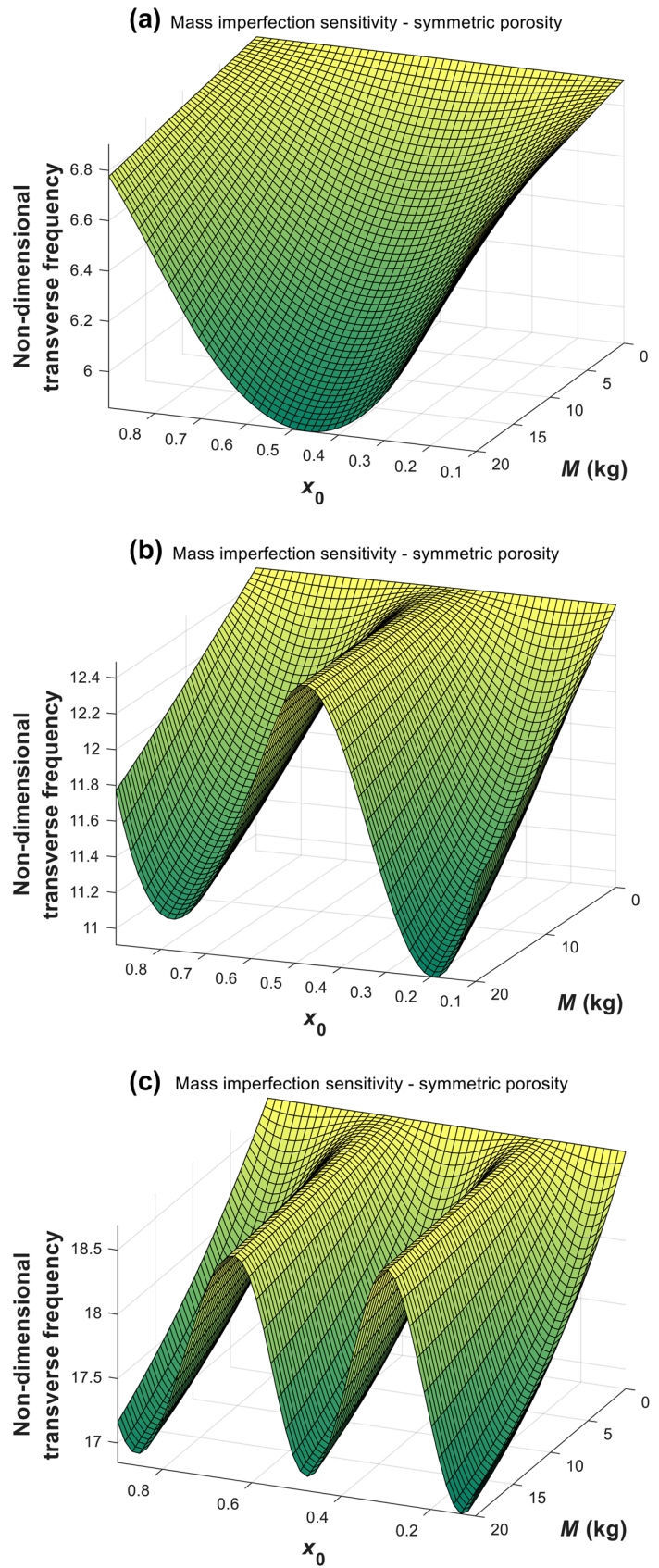


Fig. 11 Influence of mass imperfection on the first three vibration modes of the clamped–pinned symmetric porous model: (a) first natural frequency; (b) second natural frequency; (c) third natural frequency

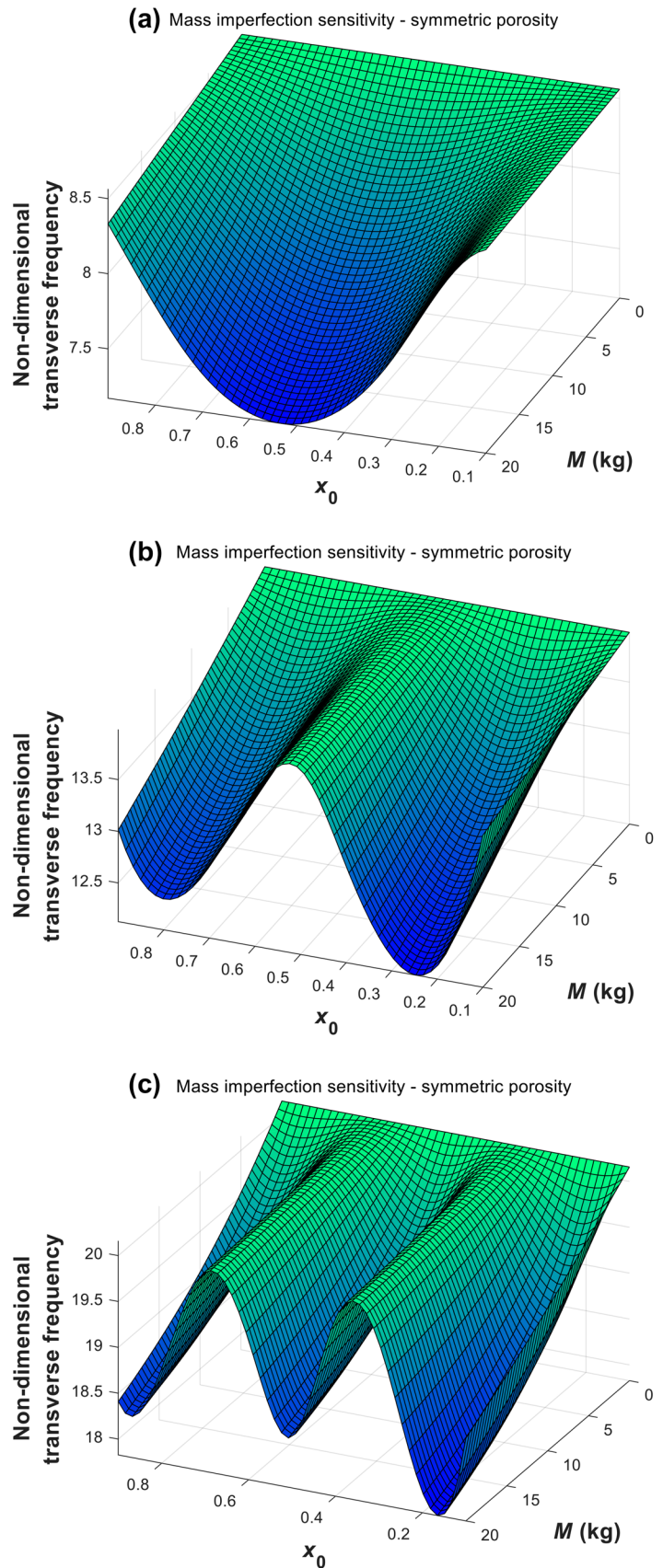


Fig. 12 Influence of mass imperfection on the first three vibration modes of the clamped–clamped linear porous model: (a) first natural frequency; (b) second natural frequency; (c) third natural frequency

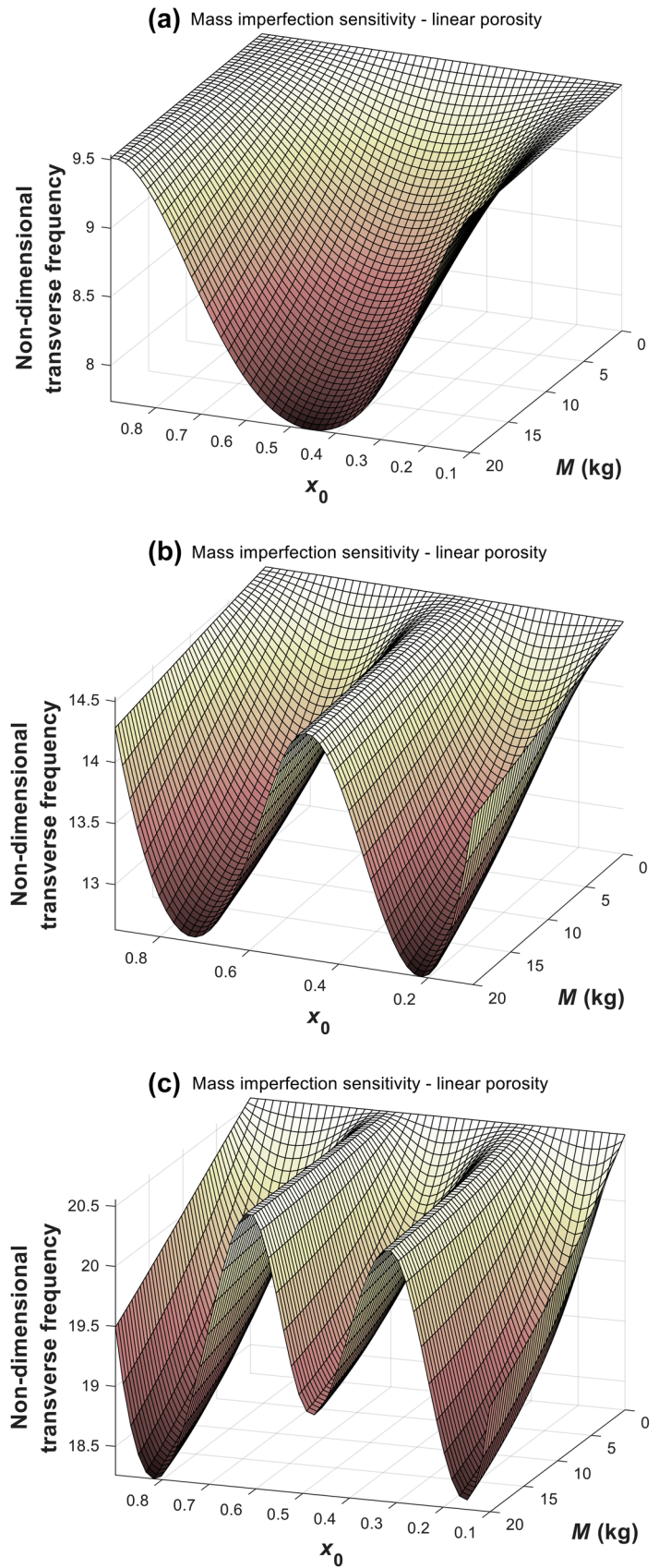
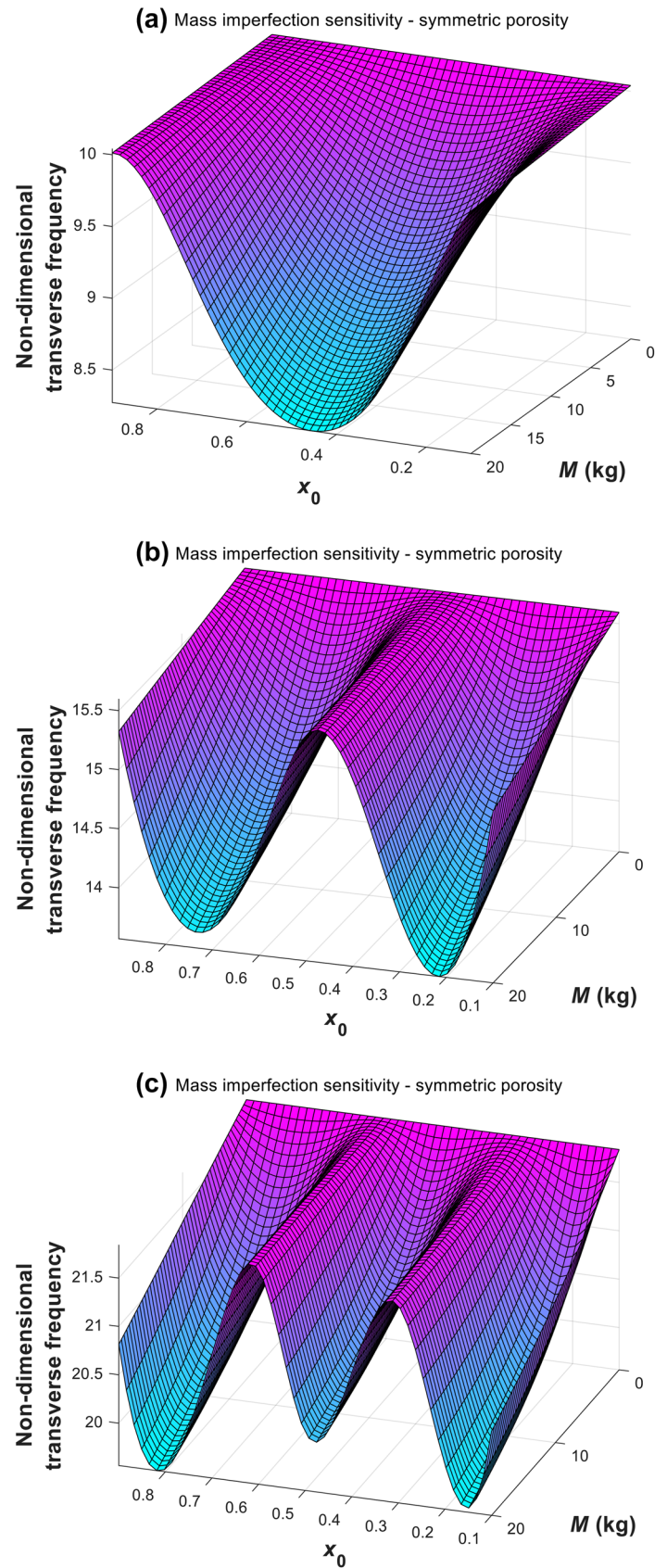


Fig. 13 Influence of mass imperfection on the first three vibration modes of the clamped–clamped symmetric porous model: (a) first natural frequency; (b) second natural frequency; (c) third natural frequency



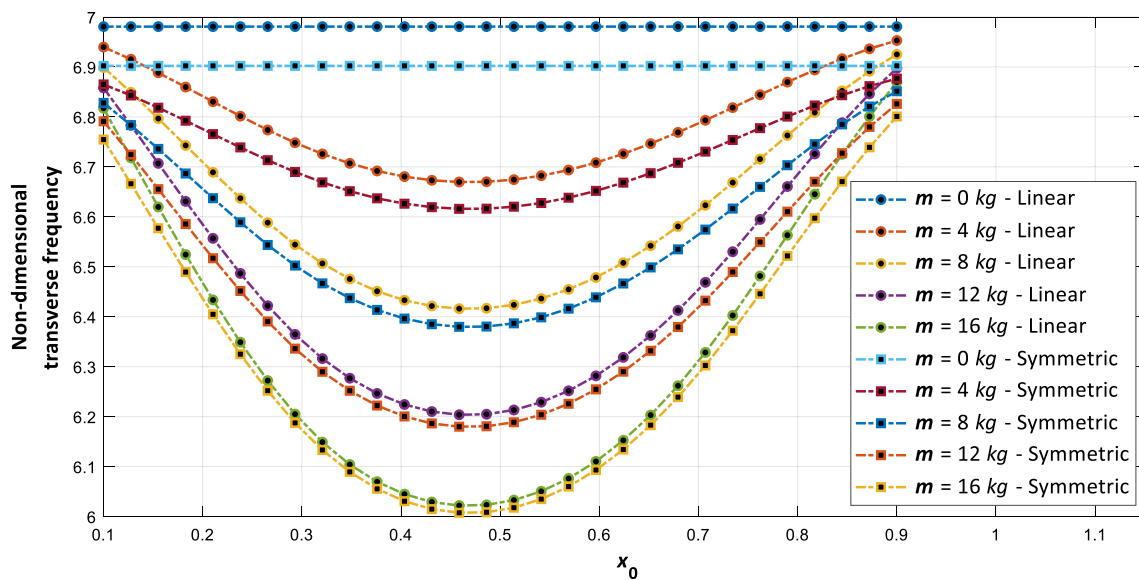


Fig. 14 Comparison between linear and symmetric porous CNT-strengthened pinned–pinned beam models in sensing mass imperfection

4.4 Influence of geometrical imperfection

Geometry imperfection plays a dominant role in varying the fundamental frequency terms of multiphase structures. Accordingly, in this subsection, the influence of considering the geometrical imperfection in obtaining vibration response is discussed. The beam is assumed with the length of 2 m, thickness of 10 cm and width of 20 cm. The total volume fraction of the CNT is varied from 0 to 5% and its volume fraction on the left side is assumed to be 0.3 of the CNT volume fraction varying through the beam with $k=2$. Porosity is varied using the nonsymmetric function presented in Eq. (11) with $\alpha_0=0.3$. Mass imperfection in the system is considered by having $x_0=0.3L$ and $m_0=10$ kg. Figures 15, 16 and 17 show the variation of the first two fundamental frequency terms for different boundary conditions by varying the geometric imperfection and CNT volume fractions. It is seen that for all the three boundary conditions, the first natural frequency term is significantly sensitive to imperfection and this sensitivity slightly increase by increasing the CNT volume fraction. The second frequency mode is less affected by the imperfection in the beam for all the boundary condition models.

4.5 Influence of CNT distribution

In this section, the role of adding CNT fibres and its distribution model in strengthening the system is discussed. By varying the CNT volume fraction through the length of the beam following

$$V(x) = RV_t(1 - x)^k + \frac{k + 1 - R}{k} V_t [1 - (1 - x)^k] , \quad (37)$$

where $V_t=0.05$ and k and R as the varying terms, the CNT distribution is as shown in Fig. 18. For this type of fibre distribution through the length, the fundamental frequency terms are obtained and presented in Fig. 19a–c for pinned–pinned, clamped–pinned and clamped–clamped models. It can be seen that increasing the CNT fibres has a significant effect in stiffening the structure. While for clamped–pinned and clamped–clamped beam models, the varying term R has higher effect in varying the frequency term; however, for the pinned–pinned model, both k and R terms show almost the same importance in varying the frequency parameter.

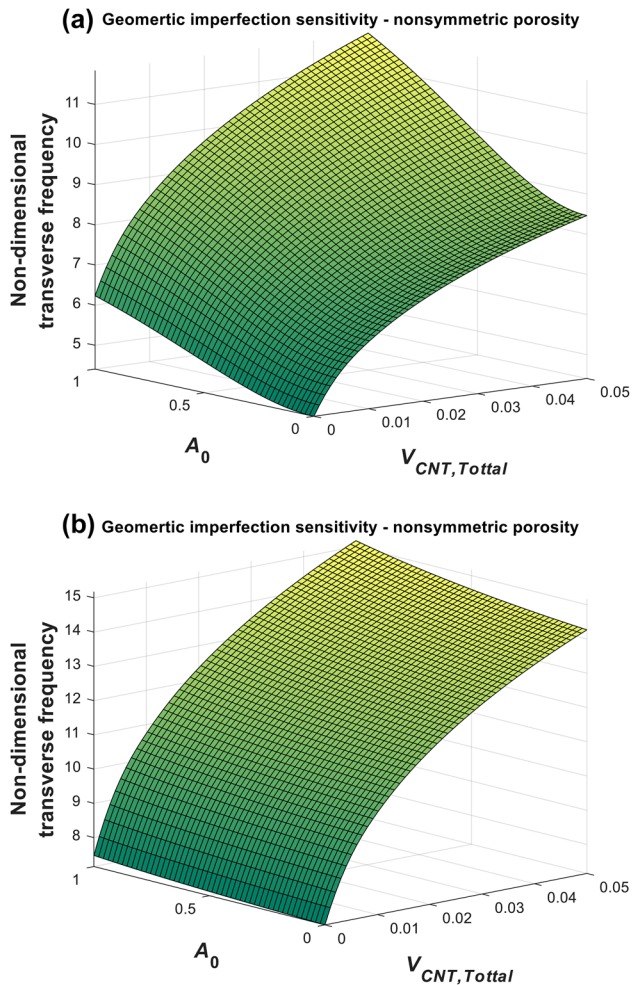


Fig. 15 Influence of the geometrical imperfection on the first two natural frequency terms for clamped-clamped non-symmetric CNT-strengthened beam model: **(a)** first mode; **(b)** second mode

5 Conclusions

A general formulation for modelling different types of imperfections (porosity, mass and geometric) in strengthened beam structures with different boundary conditions was presented in this study and the coupled vibration response of the system due to imperfections was investigated. Porosity

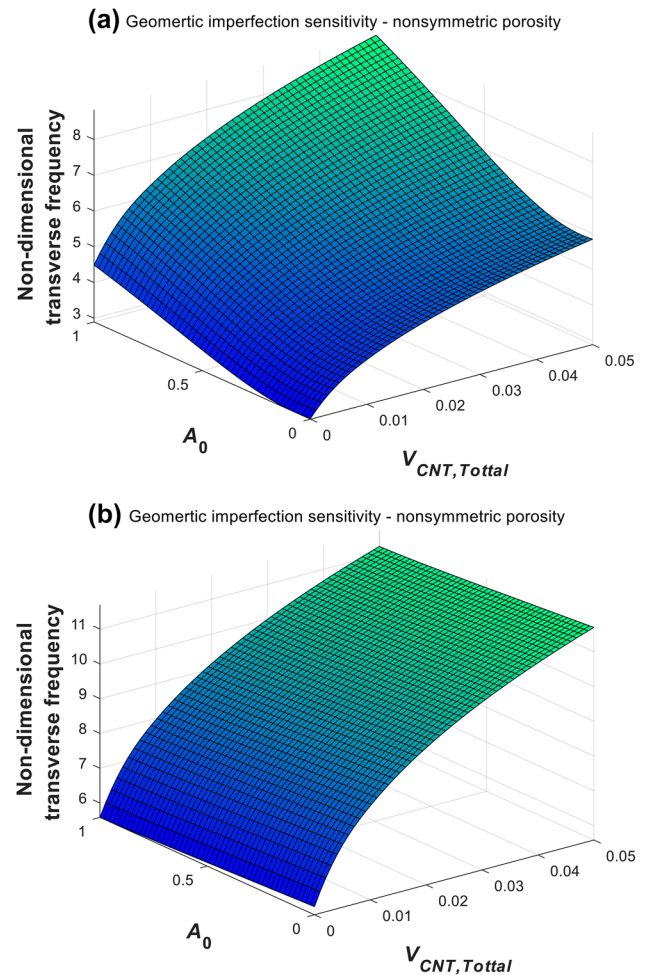


Fig. 16 Influence of the geometrical imperfection on the first two natural frequency terms for pinned-pinned non-symmetric CNT-strengthened beam model: **(a)** first mode; **(b)** second mode

was modelled using simple-cell, open-cell and closed-cell porosity models which are assumed to be uniform through the thickness of the beam or vary using linear, parabolic, symmetric and un-symmetric functions. Mass imperfection and geometry imperfection were modelled using a concentrated attached mass and initial deformation in the system. Coupled equations of motion were obtained and solved for pinned-pinned, clamped-clamped and clamped-pinned

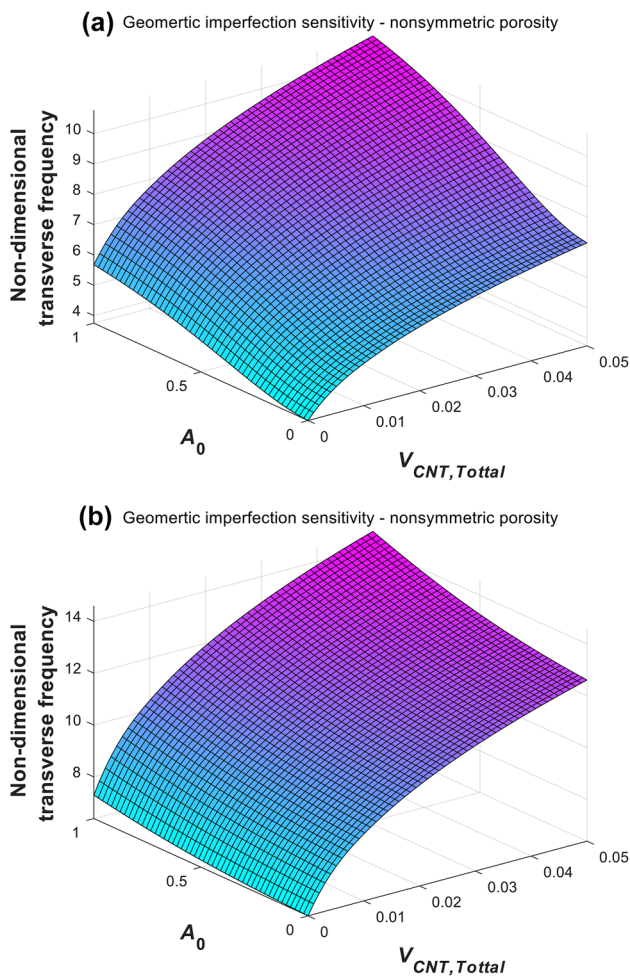


Fig. 17 Influence of the geometrical imperfection on the first two natural frequency terms for clamped–pinned non-symmetric CNT-strengthened beam model: (a) first mode; (b) second mode

imperfect CNT-strengthened beams using Hamilton’s principle and a modal decomposition technique, respectively. The current methodology is verified using FE simulation for simplified models and novel results for complicated models were presented. It was shown that:

- The porosity imperfection in the system can cause a significant effect in decreasing the natural frequency terms especially in lower modes of vibration. This effect is higher for transverse vibration compared to axial vibration response.
- It is shown that open-cell and closed-cell models give almost the same results in both trend and magnitude. However, the simple model has higher-frequency results for both the axial and transverse vibrations.
- Influence of mass imperfection is presented for different types of boundary conditions. It is shown that symmetric porous AFG imperfect CNT-strengthened model is more sensitive to mass imperfection in the system compared to linear porous models, especially for lower mass magnitudes.
- Even small imperfection can make a considerable increase in the fundamental transverse vibration response of the system; while for the axial vibration, this effect is less.
- Varying the distribution of fibres through the length can impact the imperfection effect on the system; for the studied cases, it was shown that by increasing the CNT volume fraction, the fundamental vibration frequency increases following the given distribution of fibres.

Overall, since results and discussions in this study are presented for the first time, the outcome could be used as a benchmark for further theoretical and experimental studies. Optimisation methods can also be used for further investigations to optimise the mechanical behaviour of the CNT-strengthened structures for a specific design purpose.

Fig. 18 CNT fibre volume fraction distribution through the length with respect to R and k for (a) $k=1$, (b) $k=2$, and (c) $k=5$

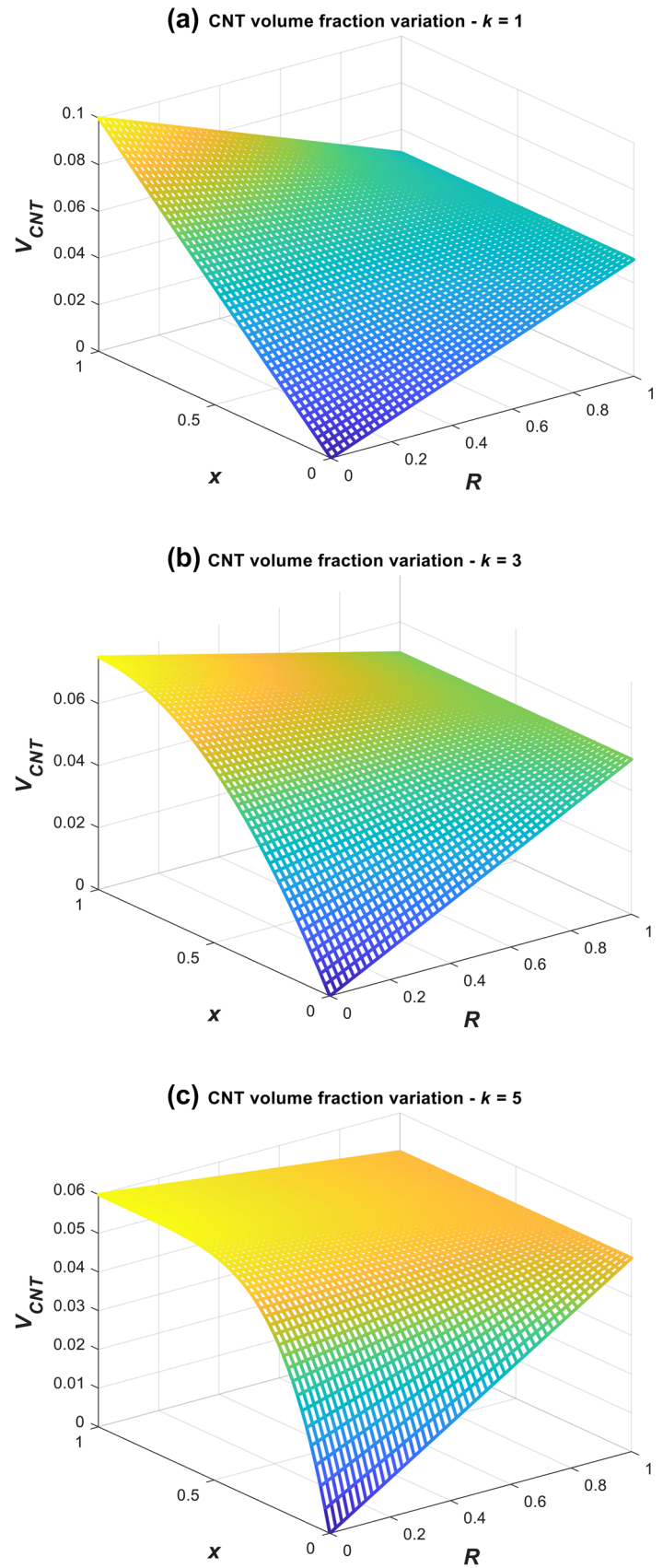
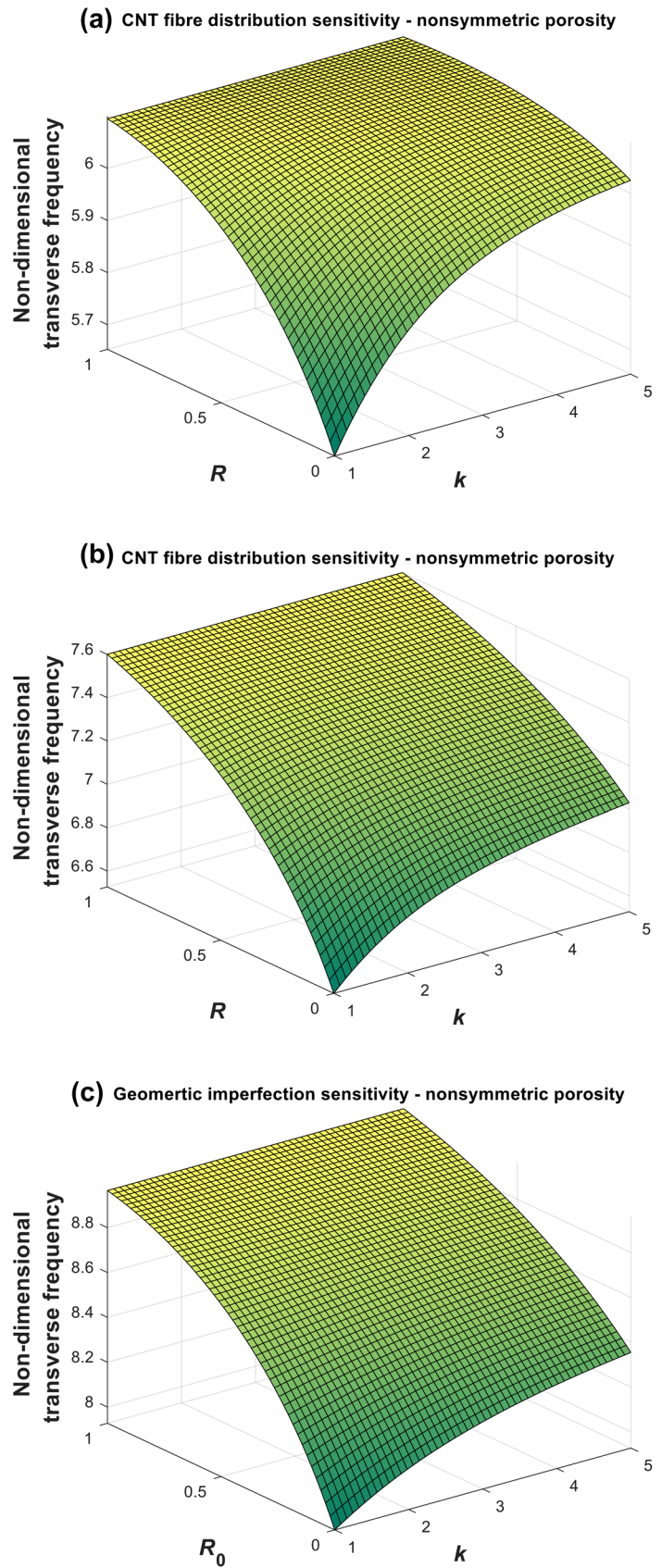


Fig. 19 Influence of CNT fibre volume fraction distribution through the length on the fundamental natural frequency term for non-symmetric porous imperfect beams **(a)** pinned–pinned, **(b)** clamped–pinned, and **(c)** clamped–clamped



References

- Matsunawa A, Mizutani M, Katayama S, Seto N (2003) Porosity formation mechanism and its prevention in laser welding. *Weld Int* 17(6):431–437
- Zhang B, Liu S, Shin YC (2019) In-Process monitoring of porosity during laser additive manufacturing process. *Addit Manuf* 28:497–505
- Zhou J, Tsai H-L (2007) Porosity formation and prevention in pulsed laser welding. *J Heat Transf* 129(8):1014–1024
- Malikan M, Eremeyev VA (2020) A new hyperbolic-polynomial higher-order elasticity theory for mechanics of thick FGM beams with imperfection in the material composition. *Compos Struct* 249:112486
- Dastjerdi S, Tadi Beni Y, Malikan M (2020) A comprehensive study on nonlinear hygro-thermo-mechanical analysis of thick functionally graded porous rotating disk based on two quasi-three-dimensional theories. *Mech Based Design Struct Mach*. <https://doi.org/10.1080/15397734.2020.1814812>
- Akgöz B, Civalek Ö (2013a) Buckling analysis of functionally graded microbeams based on the strain gradient theory. *Acta Mech* 224(9):2185–2201
- Sayyad A, Ghumare S (2019) A new quasi-3D model for functionally graded plates. *J Appl Comput Mech* 5(2):367–380
- Akgöz B, Civalek Ö (2013b) Free vibration analysis of axially functionally graded tapered Bernoulli–Euler microbeams based on the modified couple stress theory. *Compos Struct* 98:314–322
- Ghayesh MH (2019a) Viscoelastic dynamics of axially FG microbeams. *Int J Eng Sci* 135:75–85
- Ghayesh MH (2019b) Nonlinear oscillations of FG cantilevers. *Appl Acoust* 145:393–398
- Khaniki HB (2019) On vibrations of FG nanobeams. *Int J Eng Sci* 135:23–36
- Jena SK, Chakraverty S, Malikan M (2020) Application of shifted Chebyshev polynomial-based Rayleigh–Ritz method and Navier’s technique for vibration analysis of a functionally graded porous beam embedded in Kerr foundation. *Eng Comput*. <https://doi.org/10.1007/s00366-020-01018-7>
- Xie B, Sahmani S, Safaei B, Xu B (2020) Nonlinear secondary resonance of FG porous silicon nanobeams under periodic hard excitations based on surface elasticity theory. *Eng Comput*. <https://doi.org/10.1007/s00366-019-00931-w>
- Liu Z, Yang C, Gao W, Wu D, Li G (2019) Nonlinear behaviour and stability of functionally graded porous arches with graphene platelets reinforcements. *Int J Eng Sci* 137:37–56
- Akbaş ŞD (2018) Forced vibration analysis of functionally graded porous deep beams. *Compos Struct* 186:293–302
- Wu D, Liu A, Huang Y, Huang Y, Pi Y, Gao W (2018) Dynamic analysis of functionally graded porous structures through finite element analysis. *Eng Struct* 165:287–301
- Gao K, Huang Q, Kitipornchai S, Yang J (2019) Nonlinear dynamic buckling of functionally graded porous beams. *Mech Adv Mat Struct*. <https://doi.org/10.1080/15376494.2019.1567888>
- Fattahi A, Sahmani S, Ahmed N (2019) Nonlocal strain gradient beam model for nonlinear secondary resonance analysis of functionally graded porous micro/nano-beams under periodic hard excitations. *Mech Based Design Struct Mach* 48(4):403–432. <https://doi.org/10.1080/15397734.2019.1624176>
- Ebrahimi F, Farazmandnia N, Kokaba MR, Mahesh V (2019) Vibration analysis of porous magneto-electro-elastically actuated carbon nanotube-reinforced composite sandwich plate based on a refined plate theory. *Eng Comput*. <https://doi.org/10.1007/s00366-019-00864-4>
- Ebrahimi F, Dabbagh A, Taheri M (2020) Vibration analysis of porous metal foam plates rested on viscoelastic substrate. *Eng Comput*. <https://doi.org/10.1007/s00366-020-01031-w>
- Sahmani S, Fattahi A, Ahmed N (2020) Analytical treatment on the nonlocal strain gradient vibrational response of postbuckled functionally graded porous micro-/nanoplates reinforced with GPL. *Eng Comput* 36:1559–1578
- Rahmani M, Mohammadi Y, Kakavand F, Raeisifard H (2020) Vibration analysis of different types of porous FG conical sandwich shells in various thermal surroundings. *J Appl Comput Mech* 6(3):416–432
- Jena SK, Chakraverty S, Malikan M, Sedighi H (2020) Implementation of Hermite–Ritz method and Navier’s technique for vibration of functionally graded porous nanobeam embedded in Winkler–Pasternak elastic foundation using bi-Helmholtz nonlocal elasticity. *J Mech Mat Struct* 15(3):405–434
- Malikan M, Tornabene F, Dimitri R (2018) Nonlocal three-dimensional theory of elasticity for buckling behavior of functionally graded porous nanoplates using volume integrals. *Mat Res Express* 5(9):095006
- Dastjerdi S, Malikan M, Dimitri R, Tornabene F (2021) Nonlocal elasticity analysis of moderately thick porous functionally graded plates in a hygro-thermal environment. *Compos Struct* 255:112925
- Akbaş Ş, Fageehi Y, Assie A, Eltaher M (2020) Dynamic analysis of viscoelastic functionally graded porous thick beams under pulse load. *Eng Comput* 55:1–13
- Alambeigi K, Mohammadimehr M, Bamdad M, Rabczuk T (2020) Free and forced vibration analysis of a sandwich beam considering porous core and SMA hybrid composite face layers on Vlasov’s foundation. *Acta Mech* 231:3199–3218
- Dat ND, Quan TQ, Mahesh V, Duc ND (2020) Analytical solutions for nonlinear magneto-electro-elastic vibration of smart sandwich plate with carbon nanotube reinforced nanocomposite core in hygrothermal environment. *Int J Mech Sci* 186:105906
- Chen D, Kitipornchai S, Yang J (2016) Nonlinear free vibration of shear deformable sandwich beam with a functionally graded porous core. *Thin-Walled Struct* 107:39–48
- Fazzolari FA (2018) Generalized exponential, polynomial and trigonometric theories for vibration and stability analysis of porous FG sandwich beams resting on elastic foundations. *Compos B Eng* 136:254–271
- Liu Y, Su S, Huang H, Liang Y (2019) Thermal-mechanical coupling buckling analysis of porous functionally graded sandwich beams based on physical neutral plane. *Compos B Eng* 168:236–242
- Rostami R, Mohammadimehr M (2020) Vibration control of rotating sandwich cylindrical shell-reinforced nanocomposite face sheet and porous core integrated with functionally graded magneto-electro-elastic layers. *Eng Comput*. <https://doi.org/10.1007/s00366-020-01052-5>
- Hamed M, Abo-bakr R, Mohamed S, Eltaher M (2020) Influence of axial load function and optimization on static stability of sandwich functionally graded beams with porous core. *Eng Comput* 36:1929–1946
- Karimiasl M, Ebrahimi F, Mahesh V (2019) Postbuckling analysis of piezoelectric multiscale sandwich composite doubly curved porous shallow shells via Homotopy Perturbation Method. *Eng Comput*. <https://doi.org/10.1007/s00366-019-00841-x>
- Duong TM, Vu TTA, Pham DN, Nguyen DD (2020) Nonlinear post-buckling of CNTs reinforced sandwich-structured composite annular spherical shells. *Intern J Struct Stab Dyn* 20(02):2050018
- Do QC, Pham DN, Vu DQ, Vu TTA, Nguyen DD (2019) Nonlinear buckling and post-buckling of functionally graded CNTs reinforced composite truncated conical shells subjected to axial load. *Steel Compos Struct* 31(3):243–259

37. Ghayesh MH (2018a) Nonlinear vibration analysis of axially functionally graded shear-deformable tapered beams. *Appl Math Model* 59:583–596
38. Ghayesh MH (2019c) Mechanics of viscoelastic functionally graded microcantilevers. *Eur J Mech A/Solids* 73:492–499
39. Nguyen DD, Pham DN (2017) The dynamic response and vibration of functionally graded carbon nanotubes reinforced composite (FG-CNTRC) truncated conical shells resting on elastic foundation. *Materials* 10(10):1194
40. Dat ND, Khoa ND, Nguyen PD, Duc ND (2020) An analytical solution for nonlinear dynamic response and vibration of FG-CNT reinforced nanocomposite elliptical cylindrical shells resting on elastic foundations. *ZAMM J Appl Math Mech* 100(1):e201800238
41. Thanh NV, Khoa ND, Tuan ND, Tran P, Duc ND (2017) Nonlinear dynamic response and vibration of functionally graded carbon nanotube-reinforced composite (FG-CNTRC) shear deformable plates with temperature-dependent material properties and surrounded on elastic foundations. *J Therm Stresses* 40(10):1254–1274
42. Nguyen DD (2018) Nonlinear thermo-electro-mechanical dynamic response of shear deformable piezoelectric sigmoid functionally graded sandwich circular cylindrical shells on elastic foundations. *J Sandwich Struct Mater* 20(3):351–378
43. Nguyen DD, Tran QQ, Nguyen DK (2017) New approach to investigate nonlinear dynamic response and vibration of imperfect functionally graded carbon nanotube reinforced composite double curved shallow shells subjected to blast load and temperature. *Aerosp Sci Technol* 71:360–372
44. Dat ND, Quan TQ, Duc ND (2019) Nonlinear thermal vibration of carbon nanotube polymer composite elliptical cylindrical shells. *Intern J Mech Mat Design* 1–20
45. Van Thanh N, Dinh Quang V, Dinh Khoa N, Seung-Eock K, Dinh Duc N (2019) Nonlinear dynamic response and vibration of FG CNTRC shear deformable circular cylindrical shell with temperature-dependent material properties and surrounded on elastic foundations. *J Sandwich Struct Mater* 21(7):2456–2483
46. Duc ND, Nguyen PD, Cuong NH, Van Sy N, Khoa ND (2019) An analytical approach on nonlinear mechanical and thermal post-buckling of nanocomposite double-curved shallow shells reinforced by carbon nanotubes. *Proc Inst Mech Eng Part C J Mech Eng Sci* 233(11):3888–3903
47. Shafiei N, Mirjavadi SS, MohaselAfshari B, Rabby S, Kazemi M (2017) Vibration of two-dimensional imperfect functionally graded (2D-FG) porous nano-/micro-beams. *Comput Methods Appl Mech Eng* 322:615–632
48. Khaniki HB, Ghayesh MH (2020a) A review on the mechanics of carbon nanotube strengthened deformable structures. *Eng Struct* 220:110711
49. Konsta-Gdoutos MS, Metaxa ZS, Shah SP (2010) Highly dispersed carbon nanotube reinforced cement based materials. *Cem Concr Res* 40(7):1052–1059
50. Liew K, Kai M, Zhang L (2016) Carbon nanotube reinforced cementitious composites: an overview. *Compos A Appl Sci Manuf* 91:301–323
51. Yanase K, Moriyama S, Ju J (2013) Effects of CNT waviness on the effective elastic responses of CNT-reinforced polymer composites. *Acta Mech* 224(7):1351–1364
52. Ghayesh MH (2018b) Vibration analysis of shear-deformable AFG imperfect beams. *Compos Struct* 200:910–920
53. Mirjavadi SS, Forsat M, Badnava S, Barati MR (2020) Analyzing nonlocal nonlinear vibrations of two-phase geometrically imperfect piezo-magnetic beams considering piezoelectric reinforcement scheme. *J Strain Anal Eng Design* 55(7–8):258–270. <https://doi.org/10.1177/0309324720917285>
54. Wu H, Liu H (2020) Nonlinear thermo-mechanical response of temperature-dependent FG sandwich nanobeams with geometric imperfection. *Eng Comput*. <https://doi.org/10.1007/s00366-020-01005-y>
55. Malikan M, Eremeyev VA, Sedighi HM (2020) Buckling analysis of a non-concentric double-walled carbon nanotube. *Acta Mech* 231:5007–5020. <https://doi.org/10.1007/s00707-020-02784-7>
56. Malikan M (2020) On the plastic buckling of curved carbon nanotubes. *Theor Appl Mech Lett* 10(1):46–56
57. Ghayesh MH (2019d) Viscoelastic mechanics of Timoshenko functionally graded imperfect microbeams. *Compos Struct* 225:110974
58. Duc ND, Hadavinia H, Quan TQ, Khoa ND (2019) Free vibration and nonlinear dynamic response of imperfect nanocomposite FG-CNTRC double curved shallow shells in thermal environment. *Eur J Mech A/Solids* 75:355–366
59. Khaniki HB, Ghayesh MH (2020b) On the dynamics of axially functionally graded CNT strengthened deformable beams. *Eur Phys J Plus* 135(6):415
60. Wattanasakulpong N, Chaikittiratanana A (2015) Flexural vibration of imperfect functionally graded beams based on Timoshenko beam theory: Chebyshev collocation method. *Meccanica* 50(5):1331–1342
61. Gao K, Li R, Yang J (2019) Dynamic characteristics of functionally graded porous beams with interval material properties. *Eng Struct* 197:109441
62. Chen D, Yang J, Kitipornchai S (2015) Elastic buckling and static bending of shear deformable functionally graded porous beam. *Compos Struct* 133:54–61
63. Gibson I, Ashby MF (1982) The mechanics of three-dimensional cellular materials. *Proc R Soc Lond Mathe Phys Sci* 382(1782):43–59
64. Roberts AP, Garboczi EJ (2001) Elastic moduli of model random three-dimensional closed-cell cellular solids. *Acta Mater* 49(2):189–197
65. Kitipornchai S, Chen D, Yang J (2017) Free vibration and elastic buckling of functionally graded porous beams reinforced by graphene platelets. *Mater Des* 116:656–665
66. Lin F, Xiang Y (2014) Vibration of carbon nanotube reinforced composite beams based on the first and third order beam theories. *Appl Math Model* 38(15–16):3741–3754
67. Khaniki HB (2018a) On vibrations of nanobeam systems. *Int J Eng Sci* 124:85–103
68. Khaniki HB (2018b) Vibration analysis of rotating nanobeam systems using Eringen's two-phase local/nonlocal model. *Physica E* 99:310–319
69. Kutz JN, Brunton SL, Brunton BW, Proctor JL (2016) *Dynamic mode decomposition: data-driven modeling of complex systems*. SIAM, USA
70. Vega JM, Le Clainche S (2020) *Higher order dynamic mode decomposition and its applications*. Academic Press, USA
71. ANSYS® Multiphysics™, Workbench 19.2, Workbench User's Guide, ANSYS Workbench Systems, Analysis Systems, Modal